npj | Materials Degradation

www.nature.com/npjmatdeg

ARTICLE OPEN

Substitutional adsorptions of chloride at grain boundary sites on hydroxylated alumina surfaces initialize localized corrosion

Aditya Sundar[1], Ganlin Chen[1] and Liang Qi[1]✉

To understand the chloride (Cl)-induced initiation mechanism of localized corrosion of Aluminum (Al) alloys, we apply density functional theory (DFT) calculations and ab initio molecular dynamics (AIMD) simulations to investigate the interactions between Cl and hydroxylated α–Al_2O_3 surfaces, mainly (0001) orientation, under aqueous electrochemical conditions. Hydroxylated alumina surfaces thermodynamically stable in aqueous environments are constructed based on DFT calculations for both the single-crystal and bicrystal configurations. AIMD simulations suggest a Cl anion can only be stabilized on these surfaces by substituting a surface hydroxyl (OH) group. This substitution is thermodynamically favorable at sites on surface terminations of grain boundaries (GBs) in bicrystal configurations but not favorable at sites on single-crystal surfaces. Electronic structure analyses show that the different adsorption behaviors originate from the higher sensitivity of the Al–OH bond strength to the local coordination than its counterpart of the Al–Cl bond. The adsorbed Cl significantly increases the thermodynamic driving force for Al cation dissolution from alumina surfaces into the aqueous electrolyte, which can initiate localized corrosion.

npj Materials Degradation (2021)5:18; https://doi.org/10.1038/s41529-021-00161-w

INTRODUCTION

Metallic elements, such as Al, Cr, Ni, Cu, Ti, etc., are known to spontaneously develop passive oxide layers under exposure to ambient or aqueous conditions. These electronically and chemically insulating passive oxides serve as protective barriers against further metallic corrosion. However, in the presence of reactive aqueous environments containing halide species, the passive oxides undergo localized attacks by these species, possibly in an auto-catalytic mechanism, resulting in the nucleation of localized corrosion (also called pitting corrosion) sites and eventual depassivation[1–3].

Several mechanisms have been proposed to contribute to localized passivation breakdown depending on the potential distribution across the defect structures in the oxide film, such as local thinning, voiding followed by collapse, and stress-induced fracture[2,4]. A hypothesis is that the adsorption of halide species, such as chloride (Cl) anion, on the oxide surface can enhance the formation of cation vacancies and other defects, which is the first step to initiate localized corrosion[5]. According to the point defect model (PDM) proposed by Macdonald[6–12], these defects can migrate from the electrolyte/oxide interface across the oxide layer to aggregate at the metal/oxide interface, finally resulting in passive oxide breakdown. Cl itself has also been observed to penetrate the oxide layer and migrate towards the metal-oxide interface[3,13]. Experiments also suggest that defect structures such as grain boundaries, surface steps, etc., are most susceptible to Cl attack[4,14,15].

Surface sensitive experimental techniques have been extensively used to understand the nature of localized corrosion[1,4,16–19]. Scanning tunneling microscopy and atomic force microscopy studies on controlled surfaces reveal that the onset of localized passivation breakdown (with or without halide species) is more likely on surface inhomogeneities, such as grain boundaries and terraces[17]. Ni(111) surfaces passivated with bilayer NiO and Ni$(OH)_2$ were shown to be preferentially attacked at the oxide grain boundaries, forming pits of 20–30 nm lateral size and 2.2–3.8 nm depth. The presence of chloride ions in the electrolyte was shown to accelerate the growth of some pitting sites, and the emergence of larger pitting sites (30–40 nm lateral size, 5–6 nm depth). Following observations that the passive film retains its crystalline structure and the residual current increases, it was hypothesized that (1) chloride ions substitutionally replace the hydroxide ions, and (2) preferential chloride attack at step edges/grain boundaries accelerates Ni depassivation at these surface sites[20]. Controlled intergranular corrosion experiments on micro/nanocrystalline steel and Al also identify grain boundaries, triple junctions and other interfaces to be more prone to degradation[21–23]. Experimental studies of chloride-driven pitting corrosion in passivated Al have been summarized in a recent review article[24]. Spectroscopic analyses reveal the nature of interactions between Cl anions and the hydroxylated Al_2O_3 surface[24–26]. Models developed to fit X-ray absorption spectra suggest that elevated and recessed surface hydroxyl (OH) sites on α-Al_2O_3 are the most susceptible to initial attack by Cl anions, with Cl substituting the surface hydroxyl OH. Chloride has also been reported to be absorbed into the oxide and diffuse to the Al–Al_2O_3 interface[25]. Despite these reports, the detailed mechanisms, especially at the atomistic and electronic scales, driving this localized attack are not fully understood/validated.

Density functional theory (DFT) calculation provides an effective tool to investigate the atomic/electronic mechanisms of Cl-induced localized corrosion[3,27–30]. Alavi et al. investigated the thermodynamics of dissociation-adsorption of HCl molecules on the bare unsaturated (0001) basal plane of α–Al_2O_3[31]. Additionally, Petrosyan et al. studied the adsorption of Cl ions on α–Cr_2O_3 by ab initio molecular dynamics (AIMD) simulations[32]. They concluded that water molecules have minimal impact on Cl adsorption on the O-terminated surface. In a recent publication by DorMohammadi et al.[33], molecular dynamics (MD) simulations based on reactive force-field (ReaxFF) interatomic potentials were discussed to explain Cl-induced depassivation of the Fe (110) surface. While Cl was not found to penetrate the oxide surface, it aids the

[1]Department of Materials Science and Engineering, University of Michigan, Ann Arbor 48109 MI, USA. ✉email: qiliang@umich.edu

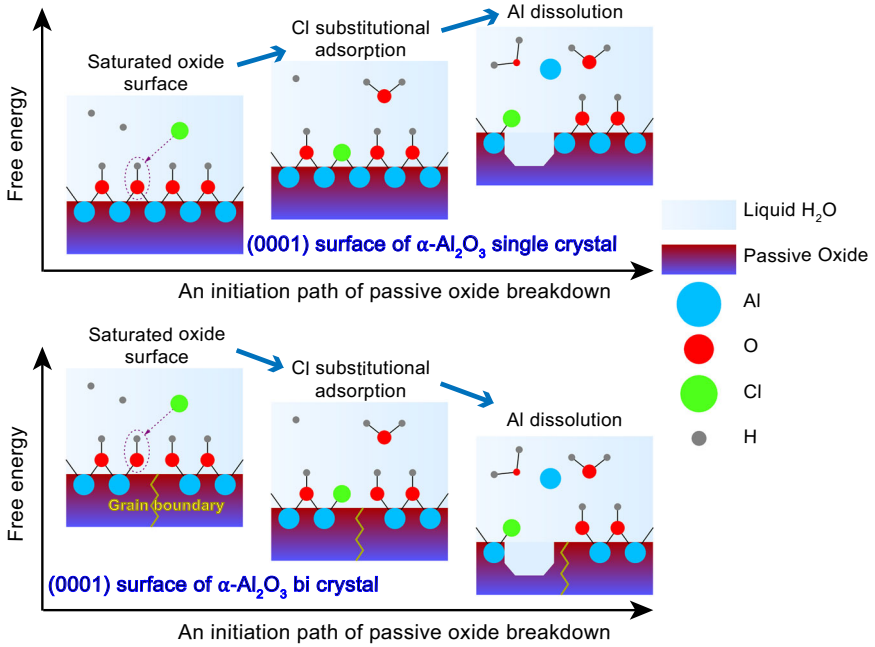

Fig. 1 Illustration of the major conclusion of this study. Under aqueous electrochemical conditions, the stable (0001) surfaces of α-Al_2O_3 are saturated with surface hydroxyl (OH). Cl can be stabilized on these surfaces only by substituting OH. This substitutional adsorption process is endothermic (thermodynamically unfavorable) on the single-crystal surface terminations (the top schematic). The adsorption process is exothermic (thermodynamically favorable) only on defect sites such as grain boundary surface terminations (the bottom schematic). The following Cl-induced Al dissolution from the passive oxide could also be exothermic only at such defect sites (the bottom schematic). A key difference between the single-crystal surface (the top schematic) and the defect sites (the bottom schematic) is the coordination number (CN) of adsorbed OH and Cl, which is defined by the number of bonds to the neighbor Al atoms on the surfaces.

formation of surface cation vacancies by the formation and subsequent dissolution of $Fe(OH)_xCl_{3-x}$ ($x = 0, 1, 2, 3$) complexes. Recent DFT studies on α–Fe_2O_3 and α–Cr_2O_3 also establish that depassivation is accelerated in the presence of aggressive chloride species[27–29,34].

One critical issue for DFT and atomistic investigations is how to accurately describe the thermodynamics of adsorption and dissolution reactions on the passive oxide surfaces at steady states in aqueous electrochemical conditions. A key factor is to generate the oxide surface configurations without the unsaturated dangling bonds because these unsaturated bonds can result in adsorption strengths that are too high for the stable surfaces passivated by reacting with water molecules. For example, Ranea et al. identified a gibbsite-like structure having a –OH termination with planar hydrogen bonds as the thermodynamically most stable surface configuration of α–Al_2O_3[35] (X-ray scattering experiments also indicate that the hydroxylated gibbsite-like surface termination is the most stable[36]). Interactions between halide species and these stable surfaces under aqueous electrochemical conditions can be significantly different from those on bare or partially hydroxylated oxide surfaces. To address this issue, Bouzoubaa et al. applied DFT calculations to study the adsorption and absorption of Cl ion on a hydroxylated NiO(111) terrace surface and surface steps[37,38]. Another critical issue is to understand the atomic/electronic mechanisms related to the effects of bulk defects, such as the surface terminations of grain boundaries, which are most susceptible to the Cl attack[4,14,15].

Here we report a comprehensive DFT + AIMD study of Cl adsorption and Cl-induced cation dissolution on α–Al_2O_3 surfaces to address the above two issues: the effects of (1) stable oxide surface structures under aqueous electrochemical conditions, and (2) surface terminations of oxide grain boundaries. The total evolution time accessed by common AIMD simulations (several picoseconds) might not be sufficient to automatically generate a fully saturated oxide surface configuration. Thus, it is essential to deliberately construct surface structures that are already thermodynamically stable under aqueous electrochemical conditions. Any electrochemical reaction involving H_2O molecules on the stable surface, such as the adsorption or desorption of either H^+ or OH^- species, should be endothermic within the H_2O stability region (electrode potential between 0 and 1.23 V with respect to the standard hydrogen electrode (SHE) at the standard condition)[39]. These stable surfaces, including the hydroxylated (0001) surfaces of both single-crystal α–Al_2O_3 and its bicrystal containing $\Sigma3(10\bar{1}0)$ grain boundaries (GBs), are presented in the first subsection of the Results section and illustrated by Fig. 1.

Based on these stable surface configurations, we sequentially present the energetic and structural variations for the dissociative adsorption of molecular HCl and the substitutional adsorption of Cl by replacing OH on these surfaces in the second subsection of the Results section and the third subsection of the Results section, respectively. In all our studied cases, free energy variations in aqueous environments show that the adsorbed Cl can be stabilized on these surfaces only by substituting OH at specific surface sites. This substitutional adsorption can be exothermic at the sites near the GB terminations but not on the perfect (0001) surfaces. The corresponding atomistic and electronic mechanisms are related to the coordination number of OH to its neighbor Al cations and discussed in detail in the Discussion section. Finally, in the fourth subsection of the Results section, we present a thermodynamic model to explain why Al cation dissolution and localized corrosion initiation can be accelerated in the presence of adsorbed Cl, especially at the surface terminations of GBs and similar defect sites where the corresponding reaction is exothermic. The corresponding atomistic and electronic mechanisms for these adsorption and dissolution reactions are discussed in the Discussion section. The key conclusions from this work are illustrated in Fig. 1. Our computational setup is described in the Methods section.

RESULTS

Surface saturation under aqueous electrochemical conditions

Accurate adsorption thermodynamics of Cl on α–Al_2O_3 surfaces in aqueous electrochemical environments can only be obtained from investigations on surface structures that are stable in the same environments. The atomistic structures of pristine α–Al_2O_3 surfaces contain O atoms with broken chemical bonds. These unsaturated surface O atoms can result in extremely strong adsorption strengths of atoms or molecules that are unrealistic in stable aqueous environments. Thus, prior to Cl adsorption calculations, the oxide surfaces (top and bottom) were first modified by adding an appropriate number of H atoms to the unsaturated surface O atoms based on a simple bond-counting scheme following Pauling's second rule[40]. On saturated surface configurations in aqueous environments at thermodynamic equilibrium, there should be no thermodynamic driving force for the electrochemical surface reactions related to hydrogen evolution or water dissociation reactions. Thus, the free energy variations of the following two electrochemical surface reactions were calculated based on DFT calculations and thermodynamic corrections.

$$S_{Al_2O_3}{-}O_nH_{l-1} + H^+_{(aq)} + e^- \rightleftharpoons S_{Al_2O_3}{-}O_nH_l \quad (1)$$

$$S_{Al_2O_3}{-}O_{n-1}H_{l-1} + H_2O_{(aq)} \rightleftharpoons S_{Al_2O_3}{-}O_nH_l + H^+_{(aq)} + e^- \quad (2)$$

Equation (1) and Eq. (2) correspond to the addition of H and OH on Al_2O_3 surfaces through hydrogen evolution and water dissociation reactions, respectively, under aqueous electrochemical conditions (denoted by the subscript (aq) for $H^+_{(aq)}$ and $H_2O_{(aq)}$ in these equations). The solid surfaces are represented by $S_{Al_2O_3}$. Italicised subscripts n and l in $S_{Al_2O_3}{-}O_nH_{l-1}$, $S_{Al_2O_3}{-}O_nH_l$ and $S_{Al_2O_3}{-}O_{n-1}H_{l-1}$ represent the number of O and H atoms on the surfaces in the simulation supercells, respectively. Equation (3) and Eq. (4) are used to calculate the Gibbs free energy variation ΔG(H) for Eq. (1). Equation (5) and Eq. (6) are used to calculate the Gibbs free energy variation ΔG(OH) for Eq. (2). To model aqueous electrochemical conditions, thermodynamic corrections, which are calculated at standard temperature and pressure (STP) conditions of 298.15 K and 1 bar, are added to the zero-K DFT energies (similar to the approaches by Norskov et al.[41]). Details are described as the following.

$$\Delta G(H) = [\mathcal{E}(S_{Al_2O_3}{-}O_nH_l)] - \left[\mathcal{E}(S_{Al_2O_3}{-}O_nH_{l-1}) + \tfrac{1}{2}\mathcal{E}(H_{2(m)}) - \tfrac{1}{2}\Delta TS_{(H_2)}\big|^{STP}_{m\to g}\right] + \Delta\mathcal{E}_{ZPE} + eU \quad (3)$$

$$\Delta\mathcal{E}_{ZPE} = \mathcal{E}_{ZPE}(-H^*) - \frac{1}{2}\mathcal{E}_{ZPE}(H_{2(m)}) \quad (4)$$

$$\Delta G(OH) = \left[\mathcal{E}(S_{Al_2O_3}{-}O_nH_l) + \tfrac{1}{2}\mathcal{E}(H_{2(m)}) - \tfrac{1}{2}\Delta TS_{(H_2)}\big|^{STP}_{m\to g}\right] - \left[\mathcal{E}(S_{Al_2O_3}{-}O_{n-1}H_{l-1}) + \mathcal{E}(H_2O_{(m)}) - \Delta TS_{(H_2O)}\big|^{STP}_{m\to g} + \Delta_{hyd}G_{(H_2O)}\big|^{STP}_{g\to aq}\right] + \Delta\mathcal{E}_{ZPE} - eU \quad (5)$$

$$\Delta\mathcal{E}_{ZPE} = \mathcal{E}_{ZPE}(-OH^*) + \frac{1}{2}\mathcal{E}_{ZPE}(H_{2(m)}) - \mathcal{E}_{ZPE}(H_2O_{(m)}) \quad (6)$$

In both Eq. (3) and Eq. (5), energy terms denoted by $\mathcal{E}$ represent the DFT calculated values at zero K. The reference energies for molecular H_2 and H_2O (denoted by the subscript (m) in Eq. (3) and Eq. (5)) were computed by relaxing isolated molecules in a large $15\times15\times15$ Å supercell. $\Delta TS\big|^{STP}_{m\to g}$ denotes the entropic correction[42] calculated from the respective translational, rotational and vibrational partition functions for the transformation from the molecular state to the gas phase (m → g) at STP conditions for H_2 and H_2O, respectively. The rotational entropy is calculated from the moments of inertia of the molecules. Linear HCl has one rotation axis perpendicular to its bond. Non-linear H_2O has three principal moments of inertia. The vibrational entropy is calculated in the harmonic oscillator approximation. For HCl, bond stretching is the only vibrational mode. For H_2O, there are three vibrational modes: symmetric bond stretch, asymmetric bond stretch and bond bending. The H_2O hydration energy $\Delta_{hyd}G_{(H_2O)}\big|^{STP}_{g\to aq}$ was obtained from Camioni et al.[43], which accounts for the transformation from the gas phase of H_2O to its aqueous phase (g → aq) at STP conditions[39]. U represents the electrode potential referenced to the standard hydrogen electrode (SHE). At SHE reference conditions (298.15 K, 1 bar, pH = 0), the free energy change for hydrogen evolution reaction ($H^+_{(aq)} + e^- \rightleftharpoons 0.5H_{2(g)}$) is 0.

In both Eq. (4) and Eq. (6), $\Delta\mathcal{E}_{ZPE}$ represents the zero point energy (ZPE) difference between the products and reactants in Eq. (3) and Eq. (5). In Eq. (4) and Eq. (6), energy terms with the asterisk * denote the ZPE for atoms/molecules adsorbed on solid surfaces. Only the ZPE corresponding to the additional adsorbed atom/molecule on the product side of Eq. (3) or Eq. (5) was calculated. All other atomic positions were frozen and not allowed to vibrate in DFT calculations of ZPE. Since Eq. (1) involves the addition of an H atom, only the ZPE of -H* was calculated. Similarly, only the ZPE of -OH* was calculated for the OH addition as Eq. (2). Other ZPE terms were calculated for isolated molecules ($H_{2(m)}$ and $H_2O_{(m)}$). In the harmonic oscillator approximation, ZPE is calculated as the sum of the energy of all real vibrational modes divided by two.

Numerical values for the all reference energies and thermodynamic corrections described from Eq. (3) to Eq. (6) are tabulated in Table 1. According these calculations, the adsorption of one additional H atom (or hydroxyl OH) on Al_2O_3 surfaces at aqueous conditions is thermodynamically favourable if the Gibbs free energy change computed by Eq. (3) (or Eq. (5)) is negative when $0 < U < 1.23$ V relative to SHE (the H_2O stability region)[39].

Figure 2(a) shows the local atomic coordination in bulk α–Al_2O_3. Each Al atom (blue) is bonded to 6 O atoms (red) as the first nearest neighbors and donates a charge of 0.5 e^- to each bond according to Pauling's second rule. Following the same rule, each O atom is bonded to 4 Al atoms as the first nearest neighbors and accepts 0.5 e^- from each bond. For our calculations, we created O-terminated surfaces and added H atoms to saturate the broken bonds to generate stable surface configurations under aqueous conditions. The hydrated configurations have been identified as the most likely surface structures from crystal truncation rod measurements at a synchrotron X-ray source[36]. Three configurations are first considered in our study, a (0001) surface of a single α–Al_2O_3 crystal and two (0001) surfaces that contain surface terminations of $\Sigma3(10\bar{1}0)$ GBs. In all the configurations, each surface layer has 12 O atoms in a supercell. For each O atom on the single-crystal surface, 2 Al–O bonds are broken and hence 1 H atom is added for the chemical saturation according to the simple bond-counting model following Pauling's second rule[40]. Figure 2 (b) shows the supercell of the single-crystal (0001) surface projected along $[\bar{1}2\bar{1}0]$, where every surface OH is bonded to 2 nearest Al atoms. Figure 2(c) shows the surface configuration projected along [0001]. The coordination number (CN) of a surface OH is defined as the number of neighboring Al atoms bonded to it and is denoted by CN. Thus, all OH have CN = 2 on the single-crystal (0001) surfaces (labeled as "2" in Fig. 2(c)).

The electrochemical stability of the crystalline surface within the H_2O stability region is presented in Fig. 2(d). Data points in Fig. 2 (d) indicate the critical value of electrode potential U_{eq}, at which the total Gibbs free energy change of the corresponding reaction (Eq. (1) or Eq. (2)) is zero. The stability region of electrode potentials ($U \in [0, 1.23]$ V) for aqueous H_2O at the standard condition (pH = 0) at the room temperature) is shaded by the light green box. The free energy for H addition is negative ($\Delta G(H) < 0$) if $U < U_{eq}$ and $\Delta G(H) > 0$, if $U > U_{eq}$. Addition of a 11th or 12th H on a

Table 1. DFT energy and thermodynamic corrections for terms from Eq. (1) to Eq. (11).

	$\mathcal{E}$(T = 0 K)	Entropy	Hydration	ZPE
HCl	−6.09	$\Delta TS_{(HCl)}\|^{STP}_{m\to g} = 0.57$	$\Delta_{hyd}G_{(HCl)}\|^{STP}_{g\to aq} = -0.37$	$\mathcal{E}_{ZPE} = 0.18$
H_2O	−14.22	$\Delta TS_{(H_2O)}\|^{STP}_{m\to g} = 0.58$	$\Delta_{hyd}G_{(H_2O)}\|^{STP}_{g\to aq} = -0.27$	$\mathcal{E}_{ZPE} = 0.56$
H_2	−6.77	$\Delta TS_{(H_2)}\|^{STP}_{m\to g} = 0.41$	0	$\mathcal{E}_{ZPE} = 0.27$
$-H^*$	–	–	–	$\mathcal{E}_{ZPE} = 0.31$
$-OH^*$	–	–	–	$\mathcal{E}_{ZPE} = 0.36$
$-Cl^*$	–	–	–	$\mathcal{E}_{ZPE} = 0.03$

All values are in eV. Hydration energies for HCl and H_2O were obtained from previous publications[43,46]. All other energy values have been computed in this work. $\mathcal{E}_{ZPE}$ for solid surfaces were computed by freezing all other atomic positions and allowing the −H*, −OH*, or −Cl* bond to vibrate. These calculations were only performed for H, OH, and Cl_{OH} adsorbed on single-crystal α–Al_2O_3 and the same corrections were used for all the surfaces.

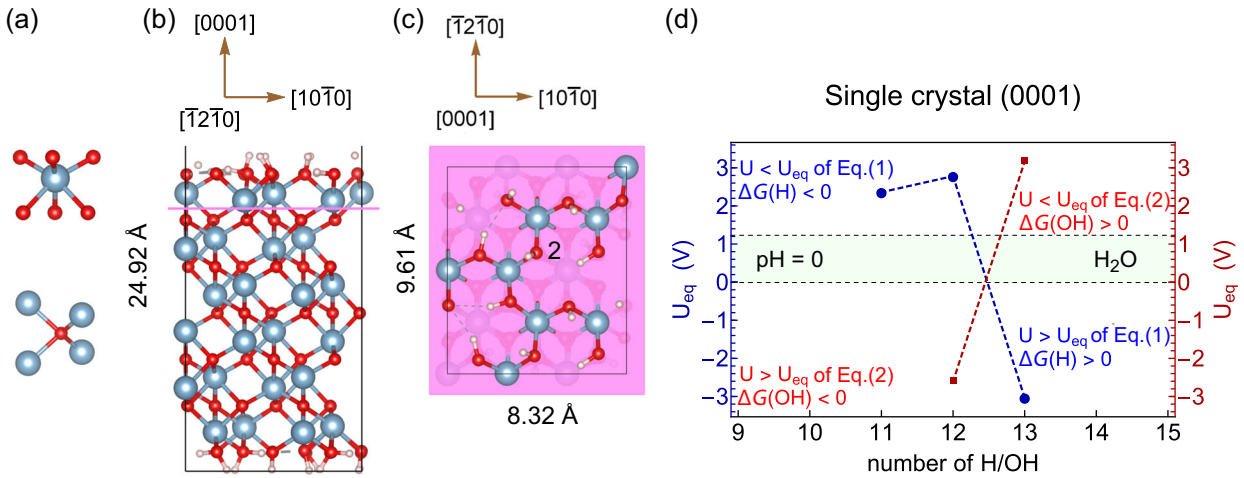

Fig. 2 The saturation of (0001) surface of single-crystal α–Al_2O_3. All atomistic structures in this paper were plotted using VESTA[55]. **a** Coordination numbers (CN) for Al (top subfigure) and O (bottom subfigure) in bulk α-Al_2O_3. Blue atoms are Al and red atoms are O. **b** Side view from the [$\bar{1}$2$\bar{1}$0] direction of the supercell that is used to simulate (0001) surface of the single-crystal α-Al_2O_3. The vacuum region is not shown here. White atoms are H. **c** Top view of the supercell in **b** projected along [0001]. The translucent magenta plane divides the top surface layers and the bulk crystal. The location of this plane is also indicated by the horizontal magenta line in **b**. Each OH on the two (0001) surfaces at the top and bottom of the supercell has CN = 2. **d** The equilibrium electrode potential U_{eq} of Eq. (1) and Eq. (2) on the (0001) surface of the supercell in **b**. The *x*-axis is the number of H/OH on the top (0001) surface of the supercell, which corresponds to the number *l* in Eq. (1) and Eq. (2). Blue and red data points are for U_{eq} of Eq. (1) and Eq. (2), respectively, calculated from Eq. (3) and Eq. (5). Within the water stability region (light green region for U ∈ [0, 1.23] V relative to SHE.), it is thermodynamically unfavorable to add a 13th H/OH on the (0001) surface of the supercell in **b**.

(0001) surface in the supercell of Fig. 2(b) and (c) is therefore thermodynamically favorable under aqueous conditions since U < U_{eq} when U ∈ [0, 1.23] eV. In other words, the corresponding U_{eq} lies above the H_2O stability region. On the other hand, addition of a 13th H on (0001) surface in the supercell is not favourable under aqueous conditions since U > U_{eq} when U ∈ [0, 1.23] V (U_{eq} lies below the water stability region).

Meanwhile, for OH adsorption in Equation (2), $\Delta G(OH) < 0$ if U > U_{eq} and $\Delta G(OH) > 0$ if U < U_{eq}. Also shown in Fig. 2(d), U > U_{eq} when U ∈ [0, 1.23] eV for the addition of a 12th OH on the (0001) surface. Hence, the 12th OH is thermodynamically stable under aqueous conditions. On the other hand, U < U_{eq} when U ∈ [0, 1.23] eV for the addition of a 13th OH. Hence, the adsorption of a 13th OH is thermodynamically unfavorable. Thus, based on either the simple bond-counting model or the detailed calculations of reaction free energies, the surface structure described in Fig. 2(b) and (c) is the thermodynamically stable configuration under aqueous electrochemical conditions. For these calculations, the 13th H/OH was added on a surface hollow site. After relaxation at zero K, the 13th H atom was bonded to a O atom (already bonded with another H) to form a H_2O molecule adsorbed on the surface. On the other hand, the 13th OH molecule bonded to a H atom and desorbed from the surface as a H_2O molecule. The corresponding configurations are shown in Supplementary Note 1.

Figure 3(a) shows the GB supercell that contains two $\Sigma3(10\bar{1}0)$ GBs (indicated by two vertical black dashed lines) terminated on the (0001) surfaces. For this particular surface cut, the OH at the GB located in the middle of the supercell is bonded to only 1 Al atom (CN = 1 and labeled as "1" in Fig. 3(b)); the OH at the GB located at the edge of the supercell is bonded to 3 Al atoms (CN = 3 and labeled as "3" in Fig. 3(b)). All other unlabeled OH in the GB supercell are bonded to 2 Al toms, similar to those on the (0001) surface of the single crystal in Fig. 2(b) and (c). We label this GB surface configuration in Fig. 3(a) and (b) as S^1_{GB}. By slicing the supercell along a different (0001) plane, a different surface configuration can be obtained, labeled as S^2_{GB} in Fig. 3(d). In S^2_{GB} as shown in Fig. 3(e), OH at the GB located at the center of the supercell has a coordination number CN = 3, and OH at the GB located at the edge of the supercell has CN = 1. All other OH have CN = 2. There are local geometric differences in the stacking of Al atoms close to the GB planes for S^1_{GB} and S^2_{GB}, but the supercells for both S^1_{GB} and S^2_{GB} have an identical number of atoms and maintain the overall bond saturation for all O atoms on the surfaces according to the same bond-counting model[40].

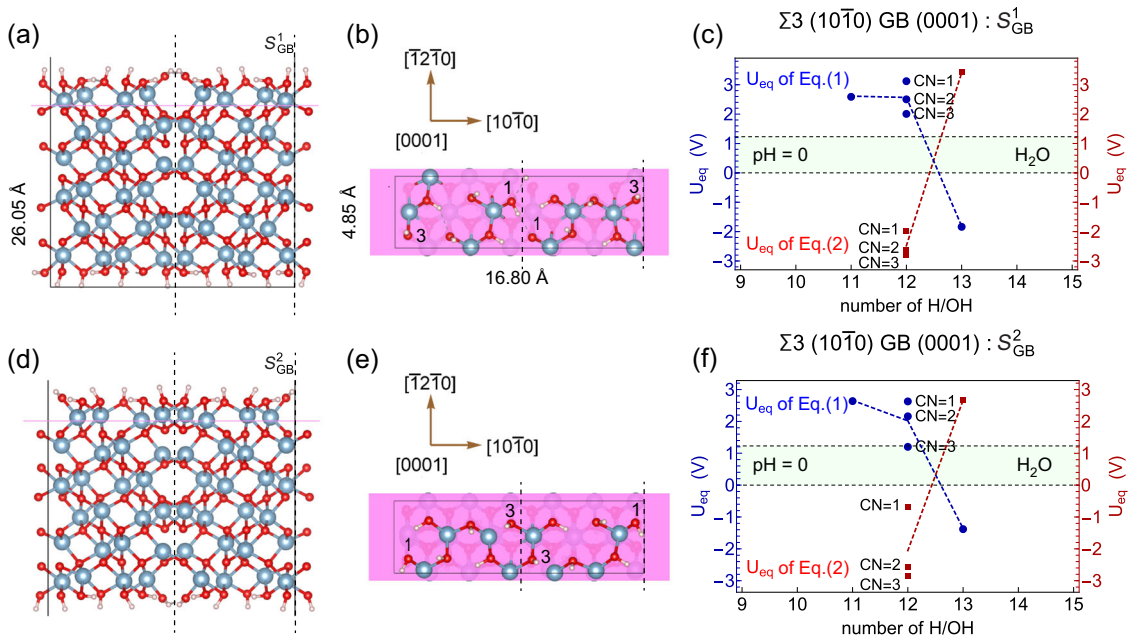

Fig. 3 Surface saturation of bicrystal α-Al_2O_3. a, b show the atomistic structure viewed from [$\bar{1}2\bar{1}0$] and [0001] of the S^1_{GB} configuration. **c** shows equilibrium electrode potential U_{eq} of Eq. (1) and Eq. (2) on (0001) surface of the S^1_{GB} configuration. The *x*-axis is the number of H/OH on the top (0001) surface of the supercell, which corresponds to the number *l* in Eq. (1) and Eq. (2). Blue and red data points are for the equilibrium potential U_{eq} of Eq. (1) and Eq.n (2), respectively, calculated based on the surface OH with different coordination numbers (CN) using Eq. (3) and Eq. (5). **d**–**f** show atomistic structure and U_{eq} for the S^2_{GB} configuration in the same ways as **a**–**c** for the S^1_{GB} configuration.

The equilibrium electrode potentials U_{eq} of Eq. (1) and Eq. (2) on the GB surface supercells are shown in Fig. 3(c) and (f) for S^1_{GB} and S^2_{GB}, respectively. Following earlier discussions for the single-crystal surface in Fig. 2(d), these results show that addition of a 13th H/OH is thermodynamically unfavorable because the corresponding U_{eq} is smaller/larger than any $U \in [0, 1.23]$ V, respectively. However, the addition of 12th H/OH at all sites irrespective of the local OH coordination is always thermodynamically favorable because the corresponding U_{eq} is larger/smaller than any $U \in [0, 1.23]$ V, respectively. Therefore, S^1_{GB} is completely saturated with 12 OH in the supercell of Fig. 3(a) under aqueous electrochemical conditions. The same conclusion can be drawn for S^2_{GB} described in Fig. 3(d), following the equilibrium electrode potentials U_{eq} of Equation (1) and Equation (2) as shown in Fig. 3 (f). For the grain boundary surface calculations, the 13th H atom was added on a surface hollow site, close to sites with CN = 2. After relaxation, the H atom was bonded to a OH at the under-coordinated CN = 1 site. Thus, an adsorbed H_2O molecule was formed on the surface. Similarly, the 13th OH molecule bonded to a H atom and desorbed from the surface as a H_2O molecule.

In a short summary, we have demonstrated that the surface configurations depicted in Figs. 2 and 3 are saturated and stable in the normal aqueous electrochemical enviroments. All the thermodynamic calculations for U_{eq} of Eq. (1) and Eq. (2) so far are conducted under the standard conditions (298.15 K, 1 bar, pH = 0). Some moderate changes in temperature, partial pressure and pH values would not affect these conclusions because most values of U_{eq} plotted in Figs. 2(d), 3(c) and (f) are far away (at least ~0.5 V in difference) from the H_2O stability region ($U \in [0, 1.23]$ V), except U_{eq} for the addition of the 12th H atom at the CN = 3 site (on S^2_{GB}) that lies on the upper boundary of the water stability region (Fig. 3 (f)). All following investigations of Cl adsorption were conducted based on surface configurations shown in Figs. 2 and 3.

It is important to note here that the nature and stability of passive oxides formed on metallic surfaces depend on aqueous pH values and electrode potential. Competitive adsorption of different species and the resultant surface coverage depends on the concentration of these species, which include H^+, OH^-, and Cl^-. Recently, a first-principles based Langmuir adsorption model[44,45] was developed to evaluate the coverage of H_2O, OH, O, and Cl on metallic surfaces, as a function of pH, electrode potential and chloride concentration. Within the Langmuir approximations—identical adsorption sites, no interaction between adsorbates—the authors provided models to evaluate the surface chemistry of metallic surfaces. In this work, we propose models to evaluate the relative sensitivity of single crystal and grain boundary surface sites on passive oxides. Reactions presented in Eq. (1) and Eq. (2) occur in acidic environments. The corresponding free energy changes in Eq. (3) and Eq. (5) are also calculated using SHE reference electrode conditions. This was chosen because the free energy change for solvation reactions (discussed later in Table 2) have been obtained from standard thermodynamic handbooks, tabulated at SHE conditions. In principle, reactions of Eq. (1) and Eq. (2) and the corresponding free energy changes can be reformulated in basic high pH environments. These calculations are discussed in Supplementary Note 2, and their results show the same stable hydroxylated structures of (0001) surfaces of both single-crystal α–Al_2O_3 and its bicrystal containing $\Sigma3(10\bar{1}0)$ GBs.

Dissociated adsorption of HCl molecule on saturated surfaces

Two mechanisms of Cl adsorption on the stable oxide surfaces (obtained from the first subsection of the Results section) were investigated: the direct adsorption of a dissociated hydrogen chloride (HCl) molecule and the substitutional adsorption of Cl by replacing an adsorbed OH on the surface. The first mechanism was studied based on the results from direct DFT and AIMD simulations, whose details are described in the Methods section. A dissociated HCl molecule was placed on the saturated (0001) surfaces (shown previously in Figs. 2 and 3) to simulate the adsorption of Cl anion on α–Al_2O_3. An isolated Cl anion was not chosen for adsorption studies because the extra electron, which is supposed to be localized surrounding the Cl, can be delocalized over the entire surface in the supercell. A neutral Cl atom was not

Table 2. Reference energies and reaction free energies described in Eq. (15) and Eq. (18) at STP conditions.

Reference reactions and cation dissolution reactions	U^0 (V)	ΔG (eV)
$Al \rightarrow Al^{3+} + 3e^-$	1.662	−4.986
$Al(OH)_3 + 3e^- \rightarrow Al + 3OH^-$	−2.30	6.93
$Al(OH)_3 \rightarrow Al^{3+} + 3OH^-$	–	1.944
$H^+ + OH^- \rightarrow H_2O$	–	−0.828
$\Delta_{hyd}G_{Al(OH)_3}\vert_{c\rightarrow aq}^{STP}$	–	−0.54
single crystal		
$\Delta G(S_{OH}^{void})$	–	2.01 (2.55)
$\Delta G(S_{Cl}^{void})$	–	1.38 (1.92)
bicrystal with GBs		
$\Delta G(S_{OH}^{void})$	–	−0.20 (0.33)
$\Delta G(S_{Cl}^{void})$	–	−0.51 (0.02)

U^0 is the equilibrium electrode potential relative to SHE for the electrochemical reference reactions[54]. For the electrochemical reactions, ΔG is the free energy change computed when U = 0 V relative to SHE at STP conditions. $\Delta_{hyd}G_{Al(OH)_3}\vert_{c\rightarrow aq}^{STP}$ is the hydration energy for crystalline Al $(OH)_3$ in the monoclinic phase as described by Eq. (13). Its value is $1.944 - 0.828 \times 3 = -0.54$ eV. $\Delta G(S_{OH}^{void})$ for Eq. (15) and $\Delta G(S_{Cl}^{void})$ for Eq. (18) denote the free energy change for the formation of a surface void after Al $(OH)_3$ dissolution without and with the Cl effect, respectively. The free energies of cation dissolution on a "single-crystal" surface and a "bicrystal with GBs" are both listed. The values in parantheses are calculated without including the hydration energy correction $\Delta_{hyd}G_{Al(OH)_3}\vert_{c\rightarrow aq}^{STP}$.

chosen since its adsorption behavior can be significantly different compared to Cl anion. Meanwhile, the charge redistribution between the adsorbed H and Cl atoms automatically achieved during DFT calculations makes our approach more appropriate to simulate the adsorption of a Cl anion on the interface between the solid electrode and the aqueous electrolyte in a finite supercell.

On the single-crystal surface, several different configurations of dissociated adsorption of a HCl molecule were considered. The top layer of O atoms has several hollow surface sites. Some of these sites are directly above an underlying Al atom. In the 1st configuration labeled as $S_{crys} - HCl^1$, the Cl atom is positioned close to the hollow sites that are not directly above Al. There are four neighboring atoms: 2 Al (2.71 and 2.99 Å away from Cl) and 2 O (1.59 and 1.70 Å away from Cl). In the 2nd configuration labeled as $S_{crys} - HCl^2$, the Cl atom is positioned 2.06 Å directly above the Al atom along [0001] direction. The Cl atom also forms three bonds with neighboring O atoms in the top layer, with bond lengths of 1.92, 1.95, and 2.00 Å, respectively. In both $S_{crys} - HCl^1$ and $S_{crys} - HCl^2$ configurations, the H atom is positioned over a hollow surface site separated by more than 4 Å from the Cl atom. After relaxation at zero K, the H atom on both surfaces remains bonded to an O atom, similar to the 13th H adsorption case described in the first subsection of the Results section. However, the Cl atom on both surfaces was found to desorb and migrate to a vertical distance of more than 2.4 Å from the (0001) surface plane along the [0001] direction, where the position of the (0001) surface plane is defined by the average coordinate of the top layer of O atom along the [0001] direction. The nearest Al atom to this Cl atom is more than 4 Å away. For comparison, the Al–Cl bond length in bulk $AlCl_3$ is 2.34 Å. The final structure for $S_{crys} - HCl^1$ is shown in Fig. 4(a).

Similar results were observed for the (0001) surface with GBs (S_{GB}^1 in Fig. 3 (a)). Two different initial configurations were considered for HCl adsorption. In $S_{GB}^1 - HCl^1$, the Cl atom is positioned close to the centre of the supercell, near an under-coordinated OH with CN = 1. The nearest atoms are 1 Al (2.19 Å away from Cl) and 3 O (1.94, 2.06, and 2.15 Å away from Cl). The H atom is placed in a hollow site far away from both of the GB interfaces. In the configuration $S_{GB}^1 - HCl^2$, Cl is placed at a hollow site close to an OH with CN = 2, and H is placed far away from both the GB interfaces. After relaxation in both configurations, Cl migrates to a distance of more than 2.4 Å from the (0001) surface plane while H is bonded to the surface.

Additionally, AIMD simulations at 300 K also produce similar results of Cl desorption from the saturated surfaces of α–Al_2O_3. Initial structures with a dissociated HCl molecule on the surface were similar to those constructed for zero-K calculations, with an additional insertion of 1.0 g/cm^3 liquid H_2O in the vacuum layer between two (0001) surfaces in the supercell. Figure 4(b) shows the final structure after 500 fs simulation for the surface. The Cl atom is far from the surface and does not form any bonds with its nearest atoms. The dynamic evolution of the bonding characteristics of Cl atoms and its distance to the (0001) surface are depicted in Fig. 4(c). In the starting configuration, the Cl atom is on a hollow site 0.62 Å above the surface measured along [0001], shown by the dashed green line in Fig. 4(c). The nearest Al atom is initially at a distance of 3.14 Å (solid green line in Fig. 4(c)). Both the values are found to increase with time, indicating the quick desorption of Cl from the surface. Similarly, the dashed and solid purple lines in Fig. 4(c) describe the Cl distance from the surface and its distance to the nearest Al atom in AIMD simulations of GB supercell S_{GB}^1 with liquid H_2O. Both lines indicate similar Cl atom desorption dynamics from the surface.

Based on all the results in Fig. 4, it can be concluded that the Cl atom from a dissociated HCl molecule can not be stable on the saturated surfaces of α–Al_2O_3 under aqueous electrochemical conditions. In the realistic interface between the solid electrode and the aqueous electrolyte, the situation can be more complex depending on many factors that are difficult to simulate by DFT in finite supercells. These factors include the accumulated charge on the interfaces, the electric field through the double-layer structures, and the partially broken solvation shell surrounding the adsorbed Cl. Nevertheless, based on the simple analyses of the bond-counting model and the confirmation of our DFT/AIMD simulations, the results suggest that the adsorption of Cl anion on α–Al_2O_3 surfaces saturated by H from the aqueous electrolyte can be so weak that thermal fluctuations at room temperature can make the Cl detached from the surfaces in a short time (within picoseconds). There should be other mechanisms for the Cl anion to be stable on the surfaces for a sufficiently long time to induce localized corrosion.

Substitutional adsorption of Cl anion on saturated surfaces

Here we describe the second mechanism of Cl adsorption (on the stable oxide surfaces obtained from the first subsection of the Results section). This was studied by substituting a surface hydroxyl –OH* with a Cl anion on one of the two surfaces in the supercell. This is mentioned in this paper as the Cl_{OH} adsorption following the concept of the Kröger-Vink notation. Because Cl and OH anions have the same nominal electronic charge, such a substitution reaction would not introduce extra polarization into the surface slab models. This Cl_{OH} adsorption reaction under the vacuum condition and its corresponding reaction energy $\Delta E(Cl_{OH})$ are described in the following.

$$S_{Al_2O_3}-O_nH_l + HCl_{(m)} \rightleftharpoons S_{Al_2O_3}-O_{n-1}H_{l-1}Cl + H_2O_{(m)} \quad (7)$$

$$\Delta E(Cl_{OH}) = \left[\mathcal{E}(S_{Al_2O_3}-O_{n-1}H_{l-1}Cl) + \mathcal{E}(H_2O_{(m)})\right] - \left[\mathcal{E}(S_{Al_2O_3}-O_nH_l) + \mathcal{E}(HCl_{(m)})\right] + \Delta\mathcal{E}_{ZPE} \quad (8)$$

$$\Delta\mathcal{E}_{ZPE} = \mathcal{E}_{ZPE}(-Cl^*) + \mathcal{E}_{ZPE}(H_2O_{(m)}) - \mathcal{E}_{ZPE}(-OH^*) - \mathcal{E}_{ZPE}(HCl_{(m)}) \quad (9)$$

Equation (7) represents the Cl_{OH} adsorption reaction that involves isolated HCl and H_2O molecules in the vacuum as the reactant and

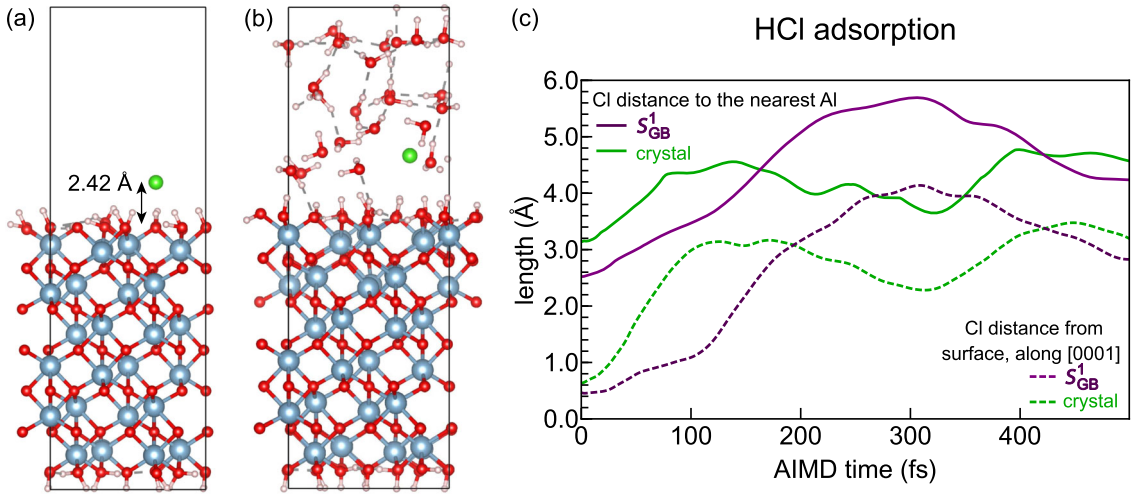

Fig. 4 Adsorption of a dissociated HCl molecule on single-crystal (0001) surface. Cl is represented by the green atom. **a** The supercell configuration after zero-K DFT minimization, where Cl is 2.42 Å away (along [0001]) from the surface defined as the top layer of O atoms. **b** The supercell configuration after 500 fs AIMD at 300 K. **c** The distance of Cl from the surface along [0001] (dashed lines) and the distance of Cl to the nearest Al atom (solid lines) for the single-crystal surface (green) and the surface with GB terminations (purple). Other simulations with different initial positions of water molecules and Cl also resulted in similar desorption processes of Cl.

the product. All energy terms in Eq. (8) and Eq. (9) were obtained from DFT calculations. $HCl_{(m)}/H_2O_{(m)}$ is represented as an isolated molecule in a $15 \times 15 \times 15$ Å supercell. The ZPE change in Eq. (9) includes the ZPE difference between the absorbed Cl^* and OH^*, which are the final and initial states for the Cl_{OH} adsorption reaction. All other symbols carry the same meaning as discussed for Eq. (1) to Eq. (6). Specifically, $S_{Al_2O_3}-O_{n-1}H_{l-1}Cl$ means the surface after the substitutional Cl_{OH} adsorption. Based on Eq. (7), the Cl_{OH} adsorption reaction under the aqueous condition and its corresponding reaction free energy $\Delta G_{aq}(Cl_{OH})$ are described in the following.

$$S_{Al_2O_3}-O_nH_l + HCl_{(aq)} \rightleftharpoons S_{Al_2O_3}-O_{n-1}H_{l-1}Cl + H_2O_{(aq)} \quad (10)$$

$$\Delta G_{aq}(Cl_{OH}) = \left[\mathcal{E}(S_{Al_2O_3}-O_{n-1}H_{l-1}Cl) + \mathcal{E}(H_2O_{(m)}) - \Delta TS_{(H_2O)}\big|^{STP}_{m\to g} + \Delta_{hyd}G_{(H_2O)}\big|^{STP}_{g\to aq}\right] - \left[\mathcal{E}(S_{Al_2O_3}-O_nH_l) + \mathcal{E}(HCl_{(m)}) - \Delta TS_{(HCl)}\big|^{STP}_{m\to g} + \Delta_{hyd}G_{(HCl)}\big|^{STP}_{g\to aq}\right] + \Delta\mathcal{E}_{ZPE} \quad (11)$$

Equation (11) represents the Gibbs free energy variation for Cl_{OH} adsorption in aqueous environments. It includes the thermodynamic corrections for the two-step transformation for both HCl and H_2O molecules. The first step includes the entropic contribution ($-\Delta TS_{(H_2O)}|^{STP}_{m\to g}$ and $-\Delta TS_{(H_2O)}|^{STP}_{m\to g}$) from the molecular state to the gas phase (m → g) at STP conditions, and the second step includes the hydration energy ($\Delta_{hyd}G_{(H_2O)}|^{STP}_{g\to aq}$ and $\Delta_{hyd}G_{(HCl)}|^{STP}_{g\to aq}$) from the gas phase to the aqueous phase (g → aq) at STP conditions. The HCl hydration energy $\Delta_{hyd}G_{(HCl)}|^{STP}_{g\to aq}$ was obtained from McGrath et al.[46]. $\Delta\mathcal{E}_{ZPE}$ in Eq. (11) is the same as calculated by Eq. (9). Numerical values for all the reference energies and thermodynamic corrections described here are also tabulated in Table 1.

We first investigate the stability of the substitutionally adsorbed Cl_{OH} on the single crystal (0001) surfaces. The substitutional Cl_{OH} configuration on (0001) surface of a single-crystal α–Al_2O_3 is shown in Fig. 5(a). The Al–Cl bond length is 2.41 Å, much smaller than the Al–Cl bond length (>4 Å) found in the dissociative adsorption of HCl molecule as shown in Fig. 4(a). Additionally, AIMD simulations at 300 K were performed for the substitutional Cl_{OH} on (0001) surfaces, where liquid H_2O with the density of 1.0 g/cm^3 is inserted in the vacuum region between two surfaces. The results confirm that the substitutional Cl_{OH} is dynamically stable close to the surface during a total simulation time of 1500 fs. The AIMD configuration after 1175 fs is shown in Fig. 5(b). Figure 5(c) shows the dynamical evolution of Al–Cl bonding characteristics. The blue line represents the Al–Cl bond length, which has an average value of 2.44 Å between 250 fs and 1250 fs, almost identical to the Al–Cl bond length from zero-K DFT relaxation in Fig. 5(a). The red line shows that Cl maintains an average position of 1.0 Å above the surface. The black circle at 1175 fs indicates the time step at which the configuration of Fig. 5 (b) is plotted.

More statistical results of AIMD simulations confirm that Cl_{OH} is dynamically stable at the surface under aqueous conditions. Figure 5(d) shows that the potential energy ($E_{potential}$) and total energy (E_{total}) of the system are stable during AIMD simulations. Their average values mentioned on the plot are obtained by averaging from 250 fs to 1250 fs. Finally, Fig. 5(e) shows the displacement of the adsorbed Cl atom along the three orthogonal axes. All the three displacement profiles exhibit sinusoidal oscillations about 0 (250–1250 fs), with an amplitude of ~0.003 Å. Other AIMD statistics including (i) the temperature variation, (ii) the Cl atom trajectory, and (iii) the comparison with the dissociated adsorption of HCl molecule are provided in Supplementary Note 3.

Next we investigate the energetic driving force of the substitutional Cl_{OH} adsorption under the vacuum and aqueous electrochemical conditions described by Eq. (7) and Eq. (10), respectively. The energy terms in Eq. (8) and Eq. (11) were computed using standard DFT calculations. From standard zero-K DFT calculation, $\Delta E(Cl_{OH}) = 0.44$ eV and $\Delta E(Cl_{OH}) = 0.75$ eV for the substitutional adsorption of 1 Cl_{OH} and 2 Cl_{OH} on the saturated (0001) surface of the single-crystal α–Al_2O_3, respectively. For the adsorption of 2 Cl atoms, we report the differential $\Delta E(Cl_{OH})$ or $\Delta G_{aq}(Cl_{OH})$ for the second Cl_{OH} adsorption using the configuration with the first Cl_{OH} adsorption as the initial state. This data are shown in Fig. 6(a), by green data points that correspond to the substitution of OH bonded with 2 neighbor Al atoms (CN = 2). Energy corrections necessary for the calculation of the Gibbs free energy change $\Delta G_{aq}(Cl_{OH})$ as described in the third subsection of the Results section are tabulated in Table 1, which shows $\Delta G_{aq}(Cl_{OH}) = \Delta E(Cl_{OH}) + 0.09$ eV at STP conditions for all adsorption sites. Thus, based on both $\Delta E(Cl_{OH})$ and $\Delta G_{aq}(Cl_{OH})$, it is not energetically favorable for the substitutional Cl_{OH} adsorption to occur on the saturated (0001) surface of the single-crystal α–Al_2O_3,

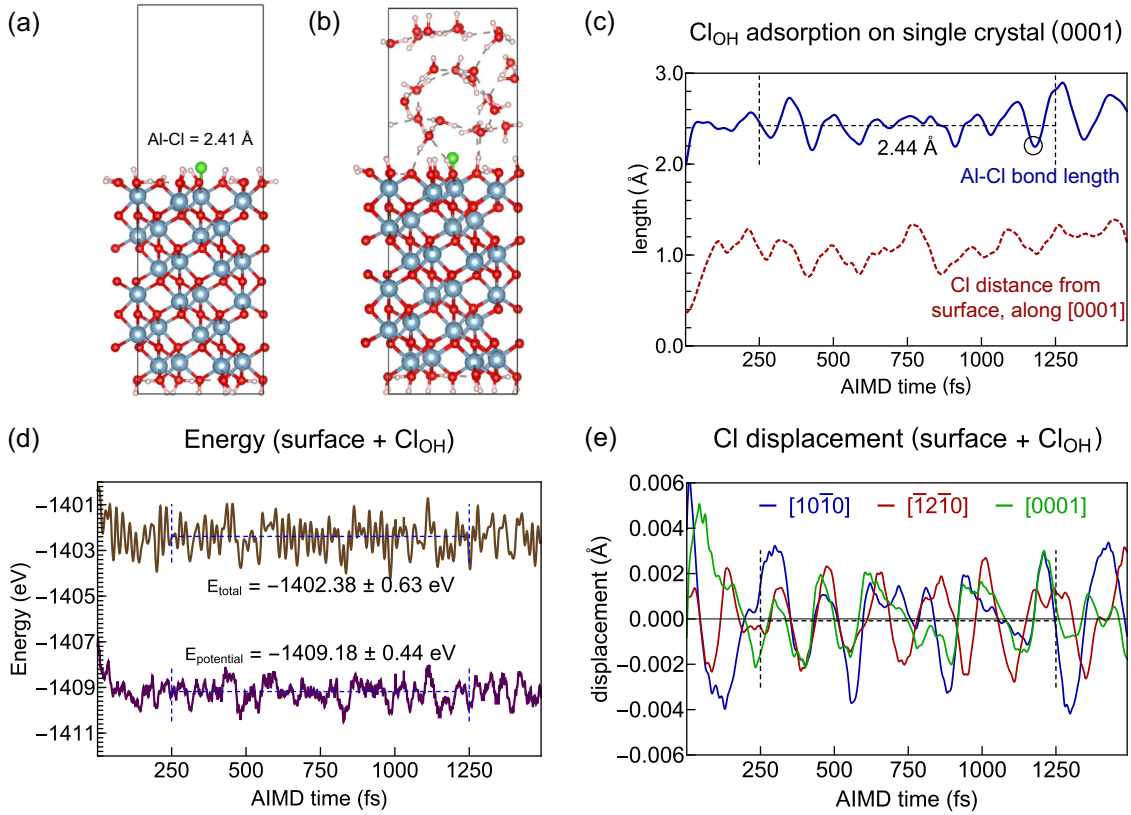

Fig. 5 Adsorption of substitutional Cl_{OH} on single-crystal (0001) surface. a Configuration after zero-K DFT minimization, **b** Configuration after 1175 fs AIMD at 300 K, **c** Al–Cl bond length (solid blue) and Cl distance from the surface along [0001] (dashed red) during the AIMD simulation in **b. d** Variation of total (E_{total}) and potential ($E_{potential}$) energy of the system and **e** the displacement of the Cl atom at each time step along the three orthogonal axes of the simulation supercell.

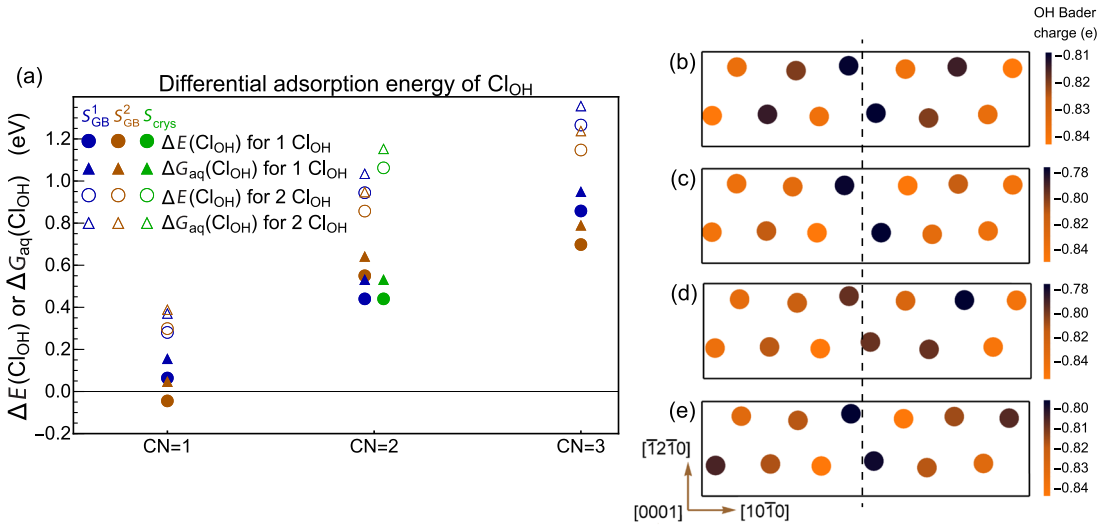

Fig. 6 Cl_{OH} adsorption energies at different surface sites. a Cl_{OH} differential adsorption energies $\Delta E(Cl_{OH})$ and $\Delta G_{aq}(Cl_{OH})$ using Eq. (8) and Eq. (11) for different OH sites on the S^1_{GB} and S^2_{GB} surfaces plotted in Fig. 3. Here the coordination number (CN) of adsorbed OH on different OH sites can change from 1 to 3. For 2 Cl cases, we report the differential $\Delta E(Cl_{OH})$ or $\Delta G_{aq}(Cl_{OH})$ for the second Cl_{OH} adsorption based on the configuration with the first Cl_{OH} adsorption. **b** Bader charges calculated for OH on S^1_{GB}. The circles on O sites represent the Bader charges of the corresponding OH molecules, with darker colors denoting lower absolute charges. **c**–**e** Bader charges for two Cl atoms substitutionally adsorbed on different OH sites (CN = 1, 2, and 3, respectively).

where each surface OH is bonded with two neighbor Al atoms (CN = 2) as shown in Fig. 2. This conclusion is true for the cases under both vacuum (Eq. (7)) and aqueous (Eq. (10)) electrochemical conditions.

Henceforth, we also perform standard DFT calculations to study the thermodynamics of the substitutional Cl_{OH} adsorption on GB surface configurations. For the S^1_{GB} and S^2_{GB} surfaces, we introduce 1 and 2 substitutional Cl_{OH} by replacing the surface OH with CN =

1, 2, 3 for a total of 12 different adsorption sites. The calculated energies are also shown in Fig. 6(a). The following discussion pertains to both S^1_{GB} and S^2_{GB} supercells plotted in Fig. 3. All the results in Fig. 6(a) demonstrate a clear trend that the adsorption strength of Cl_{OH} decreases with the increasing CN of the substituted OH because the corresponding $\Delta E(Cl_{OH})$ and $\Delta G_{aq}(Cl_{OH})$ become more positive. In addition, both $\Delta E(Cl_{OH})$ and $\Delta G_{aq}(Cl_{OH})$ can be close to zero and even have negative values only for the site with CN = 1 among all the 12 investigated cases. The substitutional Cl_{OH} adsorption becomes thermodynamically possible at these defect sites. Additionally, $\Delta G(Cl_{OH})$ for the 2nd Cl_{OH} at the CN = 1 site is still smaller than $\Delta G(Cl_{OH})$ for the 1st Cl_{OH} at CN = 2 site. In fact, all data points for the adsorption of the 2nd Cl_{OH} are shifted to higher and more positive energy values. These shifts suggests that the further adsorption of the 2nd Cl in this substitutional mechanism become thermodynamically more difficult. Thus, it could be difficult for more substitutional Cl_{OH} adsorption reaction to occur if it is thermodynamically unfavorable for the 1st Cl atom.

It is also important to discuss the effect of other parameters on the real value of the Gibbs free energy change for this adsorption process. Notably, the value of $\Delta G_{aq}(Cl_{OH})$ depends on (1) the electrolyte pH value, (2) the electrolyte chloride concentration $[Cl^-]$, (3) the interface strain effects and (4) the local atomistic structure variation due to different surface and GB orientations. Since we have formulated the substitutional adsorption Reaction Eq. (10) in acidic electrolytes, changes in aqueous pH and $[Cl^-]$ will primarily affect the HCl hydration energy in Eq. (11). Increase in pH decreases proton concentration $[H^+]$ and drives Eq. (10) to the left, increasing the value of $\Delta G_{aq}(Cl_{OH})$. Increase in $[Cl^-]$ drives Eq. (10) to the right, decreasing the value of $\Delta G_{aq}(Cl_{OH})$. Details are available in Supplementary Note 4. To model the effect of strain on adsorption thermodynamics, we performed additional calculations for the Σ3 GB configuration under bi-axial strain and the results are shown in Supplementary Note 5. The data shows that $\Delta G(Cl_{OH})$ varies approximately linearly with applied bi-axial strain along the $[10\bar{1}0]$ and $[\bar{1}2\bar{1}0]$ axes, decreasing by ~0.05 eV for every 1% increase in strain. To model the effect of atomic structures of GBs with different orientations, we also investigated the substitutional Cl_{OH} adsorption in a different surface structures: $(20\bar{2}1)$ surface with the surface terminations of $\Sigma13(10\bar{1}4)$ GBs. The adsorption energy data shows the same correlation with CN, and the value of $\Delta G_{aq}(Cl_{OH})$ is close to zero (slightly negative) at the CN = 1 sites. These results are included in Supplementary Note 6. All these calculations suggest the general trends of the substitutional Cl_{OH} adsorption as illustrated in Figs. 1 and 6(a) are robust for different atomistic structures of GBs on α–Al_2O_3 surfaces in different aqueous electrochemical environments.

To understand whether charge transfer mechanisms drive Cl_{OH} adsorption, we compare the Bader charges for anions at different surface sites before and after substitution[47–50]. We find that the change in the anion coordination number does not significantly affect the Bader charges. As seen in Fig. 6(b), OH at sites with CN = 1 have the Bader charge of $-0.80\ e^-$. The OH at sites with CN = 3 have a charge of $-0.84\ e^-$. Even though the charge difference is as small as $0.04\ e^-$, adsorption energies in Fig. 6(a) differ by around 1 eV. In Fig. 6(c–e), we plot the Bader charges after Cl_{OH} substitution at different sites. The charge distribution does not change significantly since the OH and Cl atoms both have seven valence electrons. Similar results were obtained for the S^2_{GB} configurations. Beyond Bader charge differences, in the Discussion section, we analyze detailed electronic structure mechanisms to explain the strong dependence of $\Delta E(Cl_{OH})$ and $\Delta G_{aq}(Cl_{OH})$ on the local bonding environments.

Possible effects of adsorbed Cl on alumina dissolution

After the confirmation of the thermodynamic driving forces for Cl adsorption, it is natural to ask whether and how these adsorbed Cl can accelerate the initialization of localized corrosion and whether such effects depend on the local structures of passive oxide surfaces. It has been proposed previously that the oxide film continuously dissolves and regrows at a steady state in aqueous conditions[2]. With or without Cl species, local voids are formed on the oxide surface due to the dissolution of hydroxide complexes, such as $Al(OH)_3$. It was also proposed that Cl adsorption on the weakly bonded OH sites can increase the rate of surface void formation by increasing the thermodynamic driving force for the dissolution of hydroxide–chloride complexes, such as $Al(OH)_{3-x}Cl_x$[2]. The dissolved Cl can be adsorbed again on weak OH sites to sustain the Cl supply on the void surface and promote further metal dissolution[2].

Based on these previous studies, we propose a simple reaction for Al cation dissolution and the void formation on α–Al_2O_3 surfaces. The main purpose is to verify and quantify the thermodynamic tendencies of the void formation under the effects of surface structures and chemical compositions (without or with Cl). The free energy variations of these reactions can be used as energetic indicators of whether Cl can speed up the initialization of localized corrosion on α–Al_2O_3, possibly in an auto-catalytic corrosive process[2]. For our calculations, we propose the cation dissolution reaction from the surface without the adsorbed Cl in the two following steps:

$$S_{sat} \rightleftharpoons S^{void}_{sat} + Al(OH)_{3(c)} \tag{12}$$

$$Al(OH)_{3(c)} + 3\,H^+_{(aq)} \rightarrow Al^{3+}_{(aq)} + 3H_2O_{(aq)} \tag{13}$$

Here S_{sat} represents the initial saturated surface; S^{void}_{sat} represents the final surface after one Al and its three nearest OH taken away from the surface top layer to form a surface void. The reason to choose one Al plus three OH is to make sure the surface with a void is still in the saturated state without unpaired electrons. This saturated state is confirmed by the absence of PDOS peaks at the Fermi level of the S^{void}_{sat} supercell as shown in Supplementary Fig. 8. Here we first use the crystalline structure of $Al(OH)_{3(c)}$ in Eq. (12) to describe the final state of one Al and three OH taken away from the surface, since the energy of $Al(OH)_{3(c)}$ crystal can be easily obtained by DFT calculations. Then we use Eq. (13) to transform $Al(OH)_{3(c)}$ into the dssolved state in the aqueous electrolyte. With the help of protons $H^+_{(aq)}$ in the aqueous electrolyte, the $Al(OH)_{3(c)}$ would transform into the dissolved cation $Al^{3+}_{(aq)}$ and liquid water molecules $H_2O_{(aq)}$. Thus, the total cation dissolution reaction is obtained by combining Eq. (12) and Eq. (13) into the following:

$$S_{sat} + 3H^+_{(aq)} \rightleftharpoons S^{void}_{sat} + Al^{3+}_{(aq)} + 3H_2O_{(aq)} \tag{14}$$

$$\Delta G(S^{void}_{OH}) = \mathcal{E}(S^{void}_{sat}) + \mathcal{E}(Al(OH)_{3(c)}) + \Delta_{hyd}G_{Al(OH)_3}|^{STP}_{c\rightarrow aq} - \mathcal{E}(S_{sat}) \tag{15}$$

Equation (15) is used to calculate the free energy change for the reaction in Eq. (14). Energy terms denoted by $\mathcal{E}$ are obtained from DFT calculations. The ZPE of the solid surfaces is not included here. $\mathcal{E}(Al(OH)_{3(c)})$ is the energy of its monoclinic phase (space group 14). Here its crystal structure published in the Materials Project[51–53] was used for the reference calculations of the monoclinic $Al(OH)_{3(c)}$. The hydration energy of $Al(OH)_{3(c)}$, which is defined as the reaction free energy of Eq. (13) and represented as $\Delta_{hyd}G_{Al(OH)_3}|^{STP}_{c\rightarrow aq}$ in Eq. (15), is calculated from standard electrochemical databases listed in Table 2[54]. Here, it has to been emphasized that there are other possible choices of the reference states besides Eq. (13) to transform the solid state reaction as Eq. (12) into a cation dissolution reaction in aqueous electrolyte as Eq. (14). Due to uncertainties in experimental measurements, the choices of different reference states can result in uncertainties of

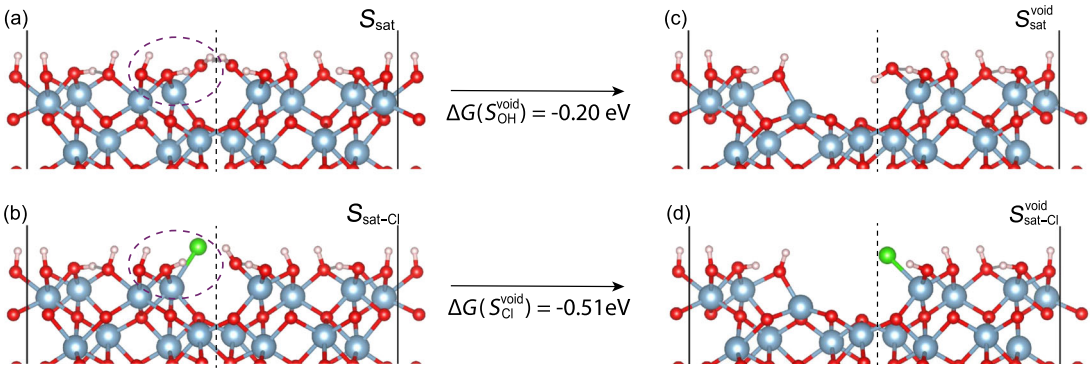

Fig. 7 Dissolution of Al cation from saturated surfaces with the GB effects. a, c show the surface structures corresponding to the terms in Eq. (14) based on the S_{GB}^{1} configuration (Fig. 3 (a)). **b, d** show the surface structures corresponding to the terms in Eq. (17) based on the S_{GB}^{1} configuration. The dashed vertical lines indicate the locations of the GB plane. For each reaction, the left configuration shows the initial saturated surface without/with Cl_{OH}, and the dashed purple ellipse includes the surface atoms that are dissolved in aqueous conditions; the right configuration shows the final states after $Al(OH)_3$ dissolution. After dissolution, the Cl atom is substitutionally adsorbed on an under-coordinated OH site (CN = 1) on the right side of the GB plane. Free energy variations calculated using Eq. (15) and Eq. (18) are indicated by relevant arrows and also tabulated in Table 2.

$\Delta G(S_{OH}^{void})$. However, it would not change the generalized tendencies of the structural and chemical effects on $\Delta G(S_{OH}^{void})$ found in this study.

Similarly, Eq. (16) and Eq. (17) represent the reaction for the void formation in the presence of a substitutionally adsorbed Cl atom as the following,

$$S_{sat-Cl} \rightleftharpoons S_{sat-Cl}^{void} + Al(OH)_{3(c)} \tag{16}$$

$$S_{sat-Cl} + 3H_{(aq)}^{+} \rightleftharpoons S_{sat-Cl}^{void} + Al_{(aq)}^{3+} + 3H_2O_{(aq)} \tag{17}$$

$$\Delta G(S_{Cl}^{void}) = \mathcal{E}(S_{sat-Cl}^{void}) + \mathcal{E}(Al(OH)_{3(c)}) + \Delta_{hyd}G_{Al(OH)_3}|_{c\rightarrow aq}^{STP} - \mathcal{E}(S_{sat-Cl}) \tag{18}$$

In these two equations, $S_{sat\text{-}Cl}$ means the Cl is already substitutionally adsorbed on the saturated surface before the dissolution reaction; S_{sat-Cl}^{void} signifies that Cl is still substitutionally adsorbed on an OH site after the cation dissolution and the void formation. Similar to Eq. (15), the free energy of cation dissolution with the adsorbed Cl effect can be written as Eq. (18). Here $\Delta_{hyd}G_{Al(OH)_3}|_{c\rightarrow aq}^{STP}$ is the same hydration energy of $Al(OH)_{3(c)}$ described by Eq. (13) and calculated from standard electrochemical databases listed in Table 2[54].

Next, we demonstrate the thermodynamics of cation dissolution and the subsequent void formation on different surfaces. first, we investigate single-crystal surfaces without GB effects. The atomistic structures before and after the void formation on the (0001) surface of the single-crystal α–Al_2O_3 are shown in Supplementary Note 7. On this single-crystal surface, the free energy change to create a surface void by the dissolution of Al cation as Equation (14) is $\Delta G(S_{OH}^{void}) = 2.01$ eV, tabulated in Table 2. In the presence of Cl, the free energy change of Equation (17) is $\Delta G(S_{Cl}^{void}) = 1.38$ eV. Although Cl can significantly reduce the endothermic tendency of cation dissolution by decreasing the positive free energy, $\Delta G(S_{Cl}^{void})$ is still much higher than zero. In addition, as noted in Fig. 6(a), the free energy of Cl_{OH} adsorption $\Delta G(Cl_{OH})$ is also positive (0.54 eV) for the OH with CN = 2 on the perfect (0001) surface. Therefore, on the single-crystal surface, Cl does not play a significant role in accelerating void nucleation because of the positive free energy changes for both the substitutional adsorption and Cl-induced cation dissolution. These tendencies are also summarized in the top subfigure of Fig. 1.

We then discuss the thermodynamics of surface void formations on the bicrystal with the GB effects. Figure 7 shows the structures of saturated surfaces without/with Cl used in Eq. (14) and Eq. (17) on the bicrystal with the GB effects. Figure 7(a) represents the initial surface with OH saturation (S_{sat} in Eq. (14)) based on the S_{GB}^{1} configuration (Fig. 3(a)). The region bound by the dashed purple ellipse includes 1 Al atom and 3 OH molecules that dissolve to form a void (S_{sat}^{void} in Eq. (14)) as shown in Fig. 7(c). Figure 7(b) represents the initial surface ($S_{sat\text{-}Cl}$ in Eq. (17)) after Cl_{OH} adsorption on the surface site with CN = 1 based on the same S_{GB}^{1} configuration. The region bound by the dashed purple ellipse includes 1 Al atom, 1 Cl atom and 2 OH molecules. Initially, Al $(OH)_2Cl$ inside the dashed ellipse is dissolved to form a surface void with the same void configuration in Fig. 7(c). Next, a neighboring OH from the new void surface replaces the Cl in dissolved $Al(OH)_2Cl$ to form the dissolved $Al(OH)_3$, allowing the readsorption of Cl by substituting the OH on the new surface void as shown in Fig. 7(d), which stands for S_{sat-Cl}^{void} in Eq. (17). The PDOS calculations shown in Supplementary Fig. 8 again confirm that the final surfaces with adsorbed Cl after the void formation (S_{sat-Cl}^{void} in Eq. (16) and Eq. (17)) are saturated since no peaks are observed at the Fermi level in its PDOS plot. This Cl readsorption allows the usage of identical electrochemical reference energies ($\Delta_{hyd}G_{Al(OH)_3}|_{c\rightarrow aq}^{STP}$) in Eq. (15) and Eq. (18). In addition, the readsorption of Cl on the void surface suggests that just a small amount of Cl can always be kept on the void surface to accelerate the cation dissolution in a self-catalytic way[2].

For these GB cases, the free energy values for different surface reactions calculated from Eq. (15) and Eq. (18) are indicated by relevant arrows in Fig. 7 and listed in Table 2. For S_{GB}^{1} configuration without the adsorbed Cl as shown in Fig. 7(a) and (c), a void is formed after one Al and three OH taken from the GB site with the corresponding $\Delta G(S_{OH}^{void}) = -0.20$ eV. Thus, compared with the void formations on the surfaces of perfect single crystals, it is much easier and thermodynamically favorable to form voids on the grain boundary termination at the surface by the $Al(OH)_3$ dissolution. In addition, after Cl_{OH} adsorption as shown from Fig. 7(b) to (d), $\Delta G(S_{Cl}^{void}) = -0.51$ eV, even more negative compared with the case from Fig. 7(a) to (c). Moreover, the substitutional adsorption of Cl on the OH with CN = 1 at this GB site is also more thermodynamically possible ($\Delta G(Cl_{OH}) = 0.16$ eV according to Fig. 6(a)) compared with its counterpart on the perfect surface. Thus, Cl can further accelerate void formation at grain boundary terminations on the surface. These tendencies are also summarized in the bottom subfigure of Fig. 1.

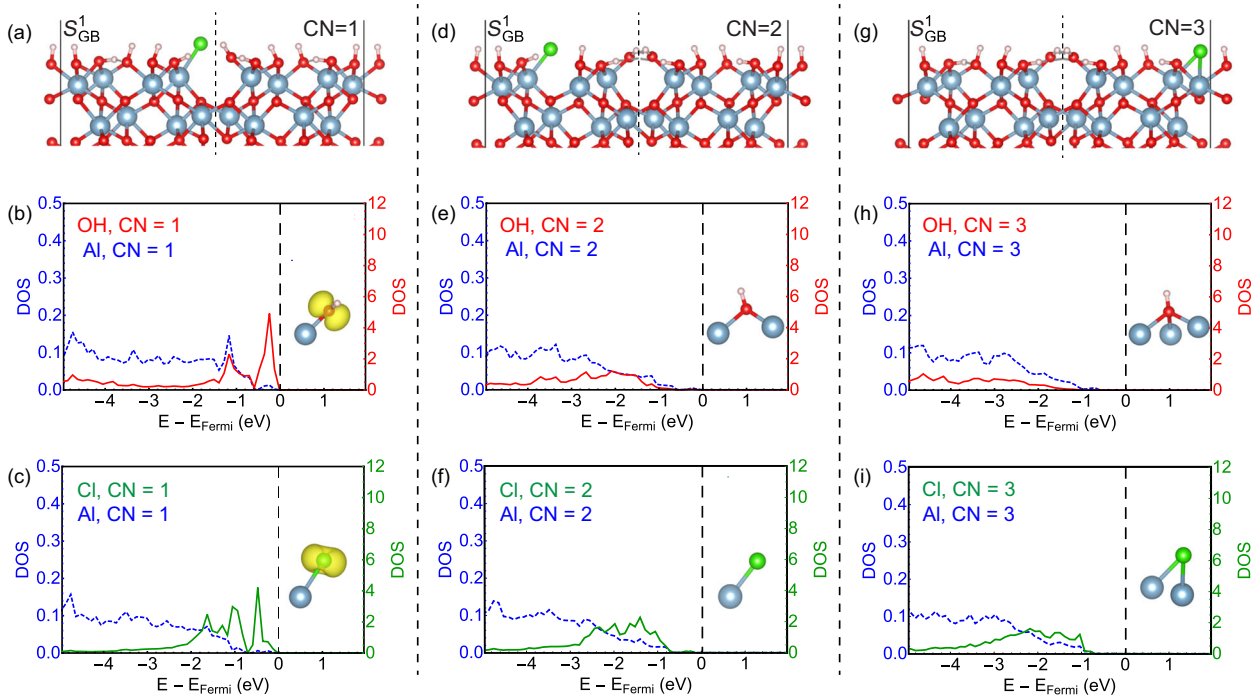

Fig. 8 Surface electronic structures for 1 Cl_{OH} at different sites. a 1 Cl_{OH} adsorbed at the OH site with CN = 1. For clarity, only atoms within two oxygen layers from the surface are shown. **b** PDOS at the CN = 1 site for the saturated surface before the Cl_{OH} adsorption. The solid red line represents the PDOS of the OH with CN = 1. The dashed blue line represents the PDOS of the Al atom that is bonded to the OH. **c** PDOS at the CN = 1 site after the Cl_{OH} adsorption. The solid green line represents the Cl atom. The dashed blue line represents the PDOS of the Al atom that is bonded to the Cl. **d**–**f** Surface configuration (**d**), the PDOS of Al/OH before the Cl_{OH} adsorption (**e**), and the PDOS of Al/Cl after the Cl_{OH} adsorption (**f**) at the site of CN = 2. **g**–**i** Surface configuration (**g**), the PDOS of Al/OH before the Cl_{OH} adsorption (**h**), and the PDOS of Al/Cl after the Cl_{OH} adsorption (**i**) at the site of CN = 3. For all PDOS plots, inset figures show the partial charge density of the anion species integrated over the PDOS peak just below the Fermi level ($E - E_{Fermi} \in [-1, 0]$ eV).

DISCUSSION

Following results described in the third subsection of the Results section, we investigated electronic structure features to explain the competitive adsorption of OH and Cl at different sites. Figure 8 presents the supercell surfaces and site projected density of electronic states (PDOS) before and after Cl_{OH} adsorption on S^1_{GB}. The surface configuration after the substitutional adsorption of 1 Cl_{OH} at the CN = 1 site is shown in Fig. 8(a). The Cl atom is bonded to 1 surface Al atom with a bond length of 2.34 Å. For reference, Fig. 3(a) shows the saturated surface and coordination environments before Cl_{OH} adsorption. The site PDOS for Al and OH before the Cl_{OH} adsorption is shown in Fig. 8(b). The PDOS of the OH at the site with CN = 1 is plotted in a solid red line. Similarly, the PDOS for the neighboring Al atom is shown by the dashed blue line. The inset figure depicts the partial charge density (PCD) integrated over the strong OH peak at approximately $E - E_{Fermi} \in [-1, 0]$ eV, where E_{Fermi} is the Fermi level. The characteristic dumbbell shape represents the p-orbital electrons. PCD calculations near the Fermi level for an isolated H_2O molecule also show a similar dumbbell like p-orbital (shown in Supplementary Note 8).

As discussed earlier in the first subsection of the Results section, 0.5 e^- is transferred in each Al–O bond in the perfect α–Al_2O_3 crystal according to the Pauling's second rule. Since 0.5 e^- can not totally saturate the OH according to the simple bond-counting model, the unbonded electron in OH contributes to the sharp PDOS peak closer to the Fermi level. In contrast, PDOS for the Al atom shows a sharp decline at ~−1 eV below the Fermi level, confirming that the sharp OH peak arises from the unbonded electron. The PDOS plots for Al and Cl after the Cl_{OH} adsorption are shown in Fig. 8(c). Similar to OH, Cl has sharp high-intensity peaks within 1 eV below the Fermi level (solid green line). In addition, compared with the peaks for OH in Fig. 8(b), the Cl PDOS peaks have stronger intensities at lower energy states for $E - E_{Fermi} \in [-2, -1]$ eV. The high PDOS value at lower energy states can be a factor why the substitution adsorption for Cl_{OH} is thermodynamically possible as shown in Fig. 6(a). The inset PCD figure shows characteristic p-orbital states for Cl. PCD calculations near the Fermi level for an isolated HCl molecule also show similar electronic states (shown in Supplementary Note 8).

In Fig. 8(d–f), surface configurations and PDOS are presented for Cl_{OH} adsorbed at the site of CN = 2. Compared to the CN = 1 site, the O atom here is bonded to 1 additional Al and the sharp peak of PDOS for OH close to the Fermi level disappears, as noted from Fig. 8(e) before the Cl_{OH} adsorption. PDOS profiles for Al show a gradual decline instead of a sharp drop. The inset figure does not depict any charge density since the intensity of electronic states within 1 eV of the Fermi level is very weak. From Fig. 8(d) after the Cl_{OH} adsorption, it is seen that the adsorbed Cl atom is bonded to 1 Al atom, with a bond length of 2.25 Å. The other Al atom is 2.75 Å away. The Cl PDOS profile in Fig. 8(f) is similar to the OH PDOS profile, with very weak intensity for $E - E_{Fermi} \in [-1, 0]$ eV. Compared to the OH PDOS, the Cl PDOS intensity is higher at the same energy level for $E - E_{Fermi} \in [-3, -1]$ eV, which is a factor why the substitutional Cl_{OH} adsorption is thermodynamically less favorable at site CN = 2 as shown in Fig. 6(a).

Finally, Fig. 8(g–i) depict the surface configurations and PDOS for Cl_{OH} adsorbed at the site of CN = 3. Since O in the OH forms four bonds (3 Al–O and 1 H–O), the PDOS of OH before the Cl_{OH} adsorption shifts to even lower energy states, as seen in Fig. 8(h). The OH PDOS completely disappears close to the Fermi level. The 3 nearest Al atoms for the Cl_{OH} are at a distance of 2.35, 2.53, and 2.67 Å as shown in Fig. 8(g). The Cl PDOS after the Cl_{OH} adsorption in Fig. 8(i) also disappears close to the Fermi level. Again, the intensity of these occupied states for Cl is higher than the PDOS

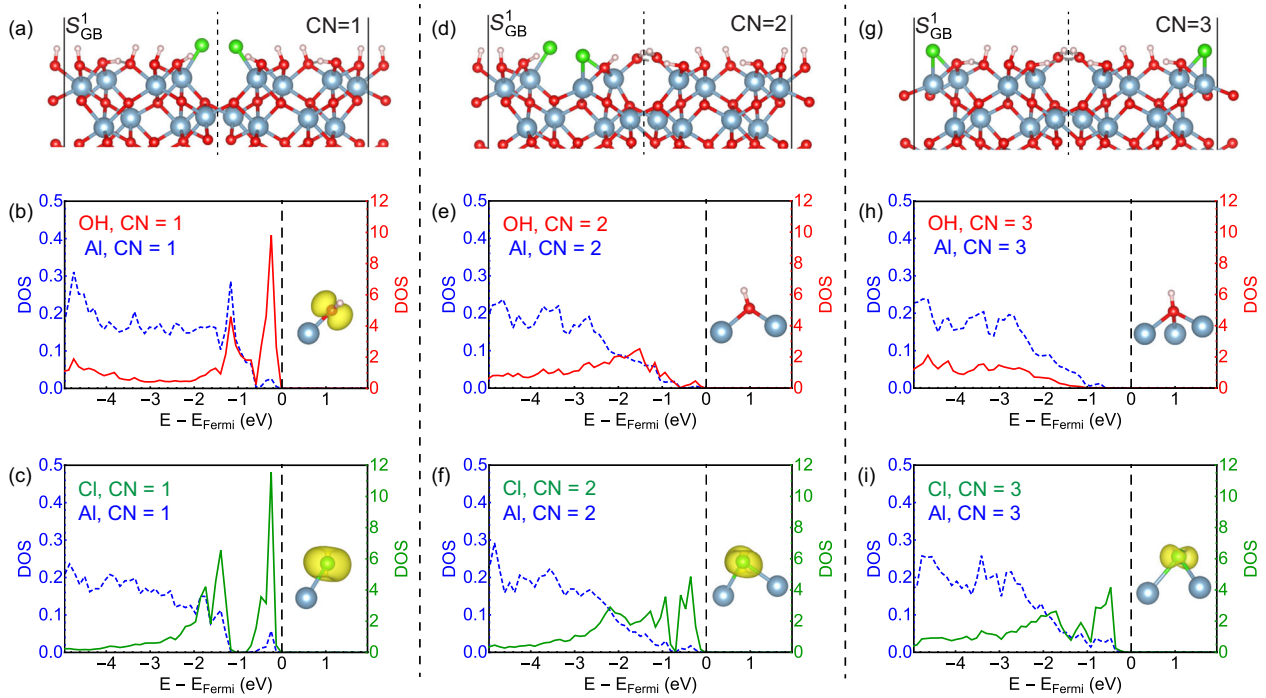

Fig. 9 Surface electronic structures for 2 Cl_{OH} at different sites. a 2 Cl_{OH} adsorbed at the OH sites with CN = 1. For clarity, only atoms within two oxygen layers from the surface are shown. **b** PDOS at the CN = 1 sites for the saturated surface before the Cl_{OH} adsorption. The solid red line represents the PDOS of the 2 OH. The dashed blue line represents the PDOS of the 2 Al that are bonded to the 2 OH. **c** PDOS at the CN = 1 sites for Cl_{OH}. The solid green line represents the 2 Cl. The dashed blue line represents the PDOS of the Al atoms that is bonded to the Cl. **d**–**f** Surface configuration (**d**), the PDOS of Al/OH before the Cl_{OH} adsorption (**e**), and the PDOS of Al/Cl after the Cl_{OH} adsorption (**f**) at the sites of CN = 2. **g**–**i** Surface configuration (**g**), the PDOS of Al/OH before the Cl_{OH} adsorption (**h**), and the PDOS of Al/Cl after the Cl_{OH} adsorption (**i**) at the sites of CN = 3. For all PDOS plots, inset figures show the partial charge density of the anion species integrated over the PDOS peak just below the Fermi level ($E - E_{Fermi} \in [-1, 0]$ eV).

intensity for OH in Fig. 8(h), for $E - E_{Fermi} \in [-3, -1]$ eV. This correlates with the more positive adsorption energy $\Delta E(Cl_{OH})$, equal to 0.86 eV as shown in Fig. 6(a).

We also present the surface configurations and local electronic structures before and after the substitutional adsorption of 2 Cl_{OH} in one supercell in Fig. 9. The trends are generally the same compared with the cases of 1 Cl_{OH} in one supercell shown in Fig. 8. At the CN = 1 sites described by Fig. 9(a–c), both the OH and Cl show strong PDOS peaks from the unpaired electron just below the Fermi level ($E - E_{Fermi} \in [-1, 0]$ eV). In the energy region further away from the Fermi level, ($E - E_{Fermi} \in [-3, -1]$ eV), the peak intensities of the Cl PDOS are higher than the counterpart of the OH PDOS. This difference can also be correlated with the thermodynamic driving force for the substitutional Cl_{OH} adsorption at the CN = 1 sites shown in Fig. 6(a). For the CN = 2 and CN = 3 sites described by Fig. 9(d–i), the intensity of all PDOS peaks near the Fermi level is significantly reduced compared to the CN = 1 sites, but the Cl PDOS peaks after the Cl_{OH} adsorption have higher intensities than the OH PDOS before the Cl_{OH} adsorption for $E - E_{Fermi} \in [-1, 0]$ eV. In summary, at all the CN = 1, CN = 2, and CN = 3 sites, the Cl PDOS shows strong peaks just below the Fermi level ($E - E_{Fermi} \in [-1, 0]$ eV). Overall, all the PDOS variations plotted in Fig. 8 and 9 indicate that Al–Cl bonds are much less sensitive to the local bond environments compared to the Al–OH bonds.

To further examine the relative strength of Al–OH and Al–Cl bonds at different sites, their binding energy ΔE_{bind} was calculated by considering the energy variations for the surface reactions listed in Eq. (19) and Eq. (20).

$$S\text{–}OH + 0.5H_{2(m)} \rightarrow S + H_2O_{(m)} \quad (19)$$

$$S\text{–}Cl + 0.5H_{2(m)} \rightarrow S + HCl_{(m)} \quad (20)$$

The initial saturated surfaces are denoted as *S*-OH without the Cl_{OH} adsorption and *S*-Cl with the Cl_{OH} adsorption. The surface after removing an OH or Cl is denoted as *S*. $H_{2(m)}$, $H_2O_{(m)}$ and $HCl_{(m)}$ are H_2, H_2O, and HCl in their corresponding isolated molecular states, respectively. Other calculation details are in Supplementary Note 9. These reactions only involve the breaking of either Al–Cl bonds or Al–OH bonds at different sites on the saturated surfaces in S^1_{GB}. The S^1_{GB} configuration has been presented previously in Fig. 3. Only the zero-K energies from direct DFT calculations were considered since additional free energy corrections would not change the relative values of ΔE_{bind}. Relative to the CN = 1 site, OH is much more stable at the CN = 2 site since the ΔE_{bind} increases by 0.62 eV. The ΔE_{bind} value continually increases by 0.17 eV at CN = 3 site. However, ΔE_{bind} for Cl only increases by 0.25 eV from the CN = 1 to the CN = 2 site, and it reduces back to almost the same ΔE_{bind} value of the CN = 1 site at the CN = 3 site. Thus, from the energetic aspect, the Al–Cl bond strength is much less sensitive to the local coordination environment compared to the Al–OH bond strength. This difference explains the dependence of the substitutional Cl_{OH} adsorption strengths on the local coordination environment shown in Fig. 6.

Beyond the substitutional Cl_{OH} adsorption, we adopt a simple bond-counting scheme to explain the large difference between void formation energies on the single-crystal and grain boundary surfaces that were reported in Table 2. On the single-crystal (0001) surface, Al is bonded to 3 O atoms below and 3 OH molecules above its (0001) plane. Every OH molecule is bonded to 2 Al atoms (CN = 2). Removing an $Al(OH)_3$ unit causes the breakage of 3 Al–O bonds and 3 Al–OH bonds. In comparison, based on the structures in Fig. 7, removing an $Al(OH)_3$ unit from the grain boundary surface breaks 3 Al–O and 2 Al–OH bonds, since 1 of the surface

OH is bonded to only 1 Al atom (CN = 1). Therefore, it should be thermodynamically favorable to create a void on the grain boundary surface relative to the crystal surface. The average energy of a single Al–OH bond in bulk $Al(OH)_3$ is −1.64 eV[51–53], explaining the large energy difference of $\Delta G(S_{OH}^{void})$ values between the single-crystal cases and the GB cases tabulated in Table 2.

To explain the further decrease of the $\Delta G(S_{Cl}^{void})$ on the grain boundary site due to the Cl effect, one needs to consider the variation of the substitutional adsorption strength of Cl on OH with various local environments. If the configuration in Fig. 7(c) is used as $S_{Al_2O_3}-O_nH_l$ and the configuration in Fig. 7(d) is used as $S_{Al_2O_3}-O_{n-1}H_{l-1}Cl$ for the substitutional Cl_{OH} adsorption as Eq. (10), the corresponding $\Delta G_{aq}(Cl_{OH})$ would become more negative, equal to −0.14 eV, compared with $\Delta G_{aq}(Cl_{OH})$ (+0.16 eV as shown in Fig. 6) on the S_{GB}^1 configuration before the cation dissolution and void formation, where the configuration in Fig. 7(a) can be used as $S_{Al_2O_3}-O_nH_l$ and the configuration in Fig. 7(b) can be used as $S_{Al_2O_3}-O_{n-1}H_{l-1}Cl$ in Eq. (10). It suggests that the major driving force for the further decrease of $\Delta G(S_{Cl}^{void})$ on the grain boundary site due to the Cl effect results from the fact that the preference of Al–Cl bonding compared with the Al–OH bonding further increases on the grain boundary void site shown in Fig. 7(c) and (d). Our analyses show a correlation between Cl_{OH} adsorption energy and the surface OH coordination number (CN) in Fig. 6. However, CN of OH that is to be replaced by Cl is the same in Fig. 7 (a) and (c); it means that there should be other short-range ordering (SRO) parameters of local structures that affect the relative strengths of Al–OH/Al–Cl bonds and the Cl-induced cation dissolution tendency. To further consolidate our results, cation dissolution free energies were also computed for the $\Sigma13(10\bar{1}0)$ GB sites on $(20\bar{2}\bar{1})$ surface. The data shown in Supplementary Note 10 also indicate that the presence of Cl accelerates the dissolution reaction at the GB sites. These findings are consistent with experimental observations that GB surface terminations are vulnerable with or without Cl, and that Cl accelerates passivation breakdown[20].

Quantification of the effect of local SRO parameters on Cl-induced cation dissolution is critical for understanding the initial stage of localized corrosion. So far the void formation in our studies is just related to the dissolution of one unit of $Al(OH)_3$. The realistic void formation is completed by the dissolution of a large amount of $Al(OH)_3$. Whether localized corrosion can be initialized highly depends on the preferred reaction directions of these multiple dissolution reactions. For the GB cases, after the first void formation, as shown in Fig. 7, localized corrosion is more likely to be initialized if the following dissolution reaction prefers to occur along the GB plane to penetrate the whole passive oxide layer, instead of layer by layer dissolution of the passive oxide and more homogeneous corrosion. Whether further dissolution can occur along the GB plane could be strongly affected by the detailed GB structures and void surface structures. Based on current studies, these preferences are related to the relative strengths of Al–OH and Al–Cl bonds. Moreover, since the structure of Fig. 7(c) contains more "defects" compared with Fig. 7(a), it suggests again the Al–Cl bond strength is more robust compared with Al–OH bond strength due to the local structure variations. Thus, we can hypothesize that certain GB structures can introduce appropriate "defect" states, which strongly prefer Al–Cl bonds and result in anisotropic dissolution along the GB to induce localized corrosion. More systematic studies on different types of GBs and even amorphous structures of passive oxides are needed to verify this hypothesis and quantify the possible SRO parameters.

In conclusion, we have developed an atomistic model to explain the thermodynamic tendencies of the Cl-induced localized corrosion initiation on passive alumina in aqueous environments. The stable hydroxylated structures of (0001) surfaces of both single-crystal α–Al_2O_3 and its bicrystal containing $\Sigma3(10\bar{1}0)$ grain boundaries (GBs) are obtained under aqueous electrochemical conditions. Our results show that (1) Cl anion from a dissociated hydrogen chloride (HCl) molecule is not stably adsorbed on these saturated surfaces, (2) Cl anion can be stabilized on these surfaces by substituting a hydroxyl (OH) that bonds with surface Al cations, and (3) local changes in the bonding environment of surface sites can change the thermodynamic driving forces of the substitutional adsorption of Cl at OH sites. Surface sites with under-coordinated OH at surface terminations of GBs are particularly vulnerable to Cl substitution. The substitutional adsorption of Cl further promotes $Al(OH)_3$ dissolution reaction to form a surface void, thereby initializing a catalytic process of localized corrosion. Similar trends are also observed for stable hydroxylated $(20\bar{2}\bar{1})$ surface containing $\Sigma13(10\bar{1}4)$ GBs. These findings are in agreement with experiments that indicate that defect sites, such as grain boundaries, surface steps, etc., are more likely to be attacked by corrosive halide anions[4,14,15].

Based on these mechanisms, corrosion inhibition strategies could be achieved by stabilizing these vulnerable sites by introducing alloying elements with the following target properties. The alloying element should segregate to the oxide surface and (1) prevent the substitutional adsorption of Cl on OH sites or (2) reduce the thermodynamic driving force for the cation dissolution reaction after Cl_{OH} adsorption. Our current analyses suggest the Cl-induced effects should result from the fact that Al–Cl bond strength is more robust against local structure variations, compared to the Al–OH bond strength. So the ideal alloying elements should be thermodynamically stable in these oxides and reduce this difference between Cl-related and OH-related chemical bonds due to certain electronic mechanisms.

METHODS

DFT relaxation at 0 K

All the calculations were performed using the Vienna Ab initio Simulation Package (VASP)[56]. The Perdew–Burke–Ernzerhof[57] (PBE) exchange–correlation functional with the projector augmented–wave method[58,59] was implemented, and 500 eV plane–wave energy cutoff was used for all the calculations. Adsorption calculations on the single-crystal α–Al_2O_3 (0001) surface were conducted in an orthogonal supercell with dimensions of 9.61 × 8.32 × 24.91 Å along $[\bar{1}2\bar{1}0]$, $[10\bar{1}0]$, and [0001], respectively. In this supercell, a (2 × 2) conventional rectangular unit cell of the hexagonal basal plane was set so that the basis vectors on the basal plane lie along the $[\bar{1}2\bar{1}0]$ and $[10\bar{1}0]$ directions. A 11.77-Å vacuum layer was inserted between two (0001) surfaces. The original supercell contains 6 oxygen (O) layers and 12 aluminum (Al) layers normal to [0001], with 2 Al layers sandwiched between each pair of O layers. In addition, to avoid polarization effects along [0001], the atoms in the bottom O layer were translated along [0001] to create a 7th O layer above the top Al layer as shown in Fig. 2(b), so the glide symmetry of the supercell slab along [0001] can eliminate the charge transfer between two surfaces to eliminate the polarization effects. A Γ-centered 3 × 3 × 2 k-point mesh was applied for this supercell.

For grain boundary (GB) adsorption calculations, a $\Sigma3(10\bar{1}0)$ GB was constructed using procedures prescribed in the literature[60,61]. The supercell size is 4.85 × 16.80 × 26.05 Å. The first 2 basis vectors along $[\bar{1}2\bar{1}0]$ and $[10\bar{1}0]$ form the basal plane of the first grain. To construct the second grain, the first grain was rotated by 180° along the $[10\bar{1}0]$ axis and then translated along $[\bar{1}2\bar{1}0]$ by 2.42 Å, which is equal to half the translational symmetry length along $[\bar{1}2\bar{1}0]$. The supercell has 2 GB planes parallel to $(10\bar{1}0)$. They are located at the centre and edge of the supercell, with local differences in the stacking sequence. Detailed atomistic structures of the GB supercell are plotted in Fig. 3. Like the single-crystal configuration, a 11.77-Å vacuum region separates the surfaces normal to [0001]. A Γ-centered 5 × 3 × 2 k-point mesh was applied for this supercell. In addition, $(20\bar{2}\bar{1})$ surface with the $\Sigma13(10\bar{1}4)$ GB terminations were constructed using procedures prescribed in the literature[62,63].

AIMD simulations at 300 K

For both the single-crystal and GB supercells, H_2O molecules were inserted to simulate the solvation effects on Cl adsorption using ab initio molecular dynamics (AIMD) simulations. The number of H_2O molecules was chosen to achieve a liquid H_2O density of 1.0 g/cm^3. All AIMD simulations were performed in the canonical NVT ensemble. The temperature was set to 300 K using a Nose–Hoover thermostat. The time step was set to 0.5 fs. For the single-crystal supercell, the dimensions of the vacuum layer between two surfaces are $9.61 \times 8.32 \times 11.77$ Å. This region was divided into a $3 \times 2 \times 4$ grid and 1 H_2O molecule was added to each grid, for a total of 24 molecules. For the grain boundary supercell, the $4.85 \times 16.80 \times 11.77$ Å vacuum region was divided into a $2 \times 4 \times 3$ grid. The O atom of each H_2O molecule was placed at the geometrical centre of each grid and the H atom coordinates were generated with arbitrary orientation, while maintaining the molecular structure of H_2O. The molecular structure of H_2O was initially optimised by relaxing a single molecule in a $15 \times 15 \times 15$ Å box. For each configuration, more than 1000 AIMD steps were performed to search the stable configurations of adsorbed Cl on α–Al_2O_3 surfaces in aqueous environments.

DATA AVAILABILITY

The data that support the findings of this study are available from the corresponding author upon reasonable request.

Received: 6 October 2020; Accepted: 8 March 2021;
Published online: 12 April 2021

REFERENCES

1. Guo, P. et al. Direct observation of pitting corrosion evolutions on carbon steel surfaces at the nano-to-micro-scales. *Sci. Rep.* **8**, 1–12 (2018).
2. Marcus, P., Maurice, V. & Strehblow, H. H. Localized corrosion (pitting): a model of passivity breakdown including the role of the oxide layer nanostructure. *Corrosion Sci.* **50**, 2698–2704 (2008).
3. Ke, H. & Taylor, C. D. Density functional theory: an essential partner in the integrated computational materials engineering approach to corrosion. *Corrosion* **75**, 708–726 (2019).
4. Maurice, V. & Marcus, P. Progress in corrosion science at atomic and nanometric scales. *Prog. Mater. Sci.* **95**, 132–171 (2018).
5. Natishan, P. 2017 wr whitney award: Perspectives on chloride interactions with passive oxides and oxide film breakdown. *Corrosion* **74**, 263–275 (2018).
6. Lin, L., Chao, C. & Macdonald, D. A point defect model for anodic passive films ii. chemical breakdown and pit initiation. *J. Electrochem. Soc.* **128**, 1194–1198 (1981).
7. Chao, C., Lin, L. & Macdonald, D. A point defect model for anodic passive films: I. film growth kinetics. *J. Electrochem. Soc.* **128**, 1187 (1981).
8. Macdonald, D. D. The point defect model for the passive state. *J. Electrochem. Soc.* **139**, 3434 (1992).
9. Lu, P., Engelhardt, G. R., Kursten, B. & Macdonald, D. D. The kinetics of nucleation of metastable pits on metal surfaces: the point defect model and its optimization on data obtained on stainless steel, carbon steel, iron, aluminum and alloy-22. *J. Electrochem. Soc.* **163**, C156–C163 (2016).
10. Li, T., Scully, J. & Frankel, G. Localized corrosion: passive film breakdown vs pit growth stability: Part ii. a model for critical pitting temperature. *J. Electrochem. Soc.* **165**, C484 (2018).
11. Li, T., Scully, J. & Frankel, G. Localized corrosion: passive film breakdown vs. pit growth stability: Part iii. a unifying set of principal parameters and criteria for pit stabilization and salt film formation. *J. Electrochem. Soc.* **165**, C762 (2018).
12. Li, T., Scully, J. & Frankel, G. Localized corrosion: passive film breakdown vs. pit growth stability: part iv. the role of salt film in pit growth: a mathematical framework. *J. Electrochem. Soc.* **166**, C115 (2019).
13. Zhang, B. et al. Unmasking chloride attack on the passive film of metals. *Nat. Commun.* **9**, 1–9 (2018).
14. Maurice, V. & Marcus, P. Passive films at the nanoscale. *Electrochim. Acta* **84**, 129–138 (2012).
15. Ma, L., Wiame, F., Maurice, V. & Marcus, P. Origin of nanoscale heterogeneity in the surface oxide film protecting stainless steel against corrosion. *npj Mater. Degrad.* **3**, 1–9 (2019).
16. Lafront, A. M. et al. Pitting corrosion of az91d and aj62x magnesium alloys in alkaline chloride medium using electrochemical techniques. *Electrochim. Acta* **51**, 489–501 (2005).
17. Marcus, P. & Maurice, V. Atomic level characterization in corrosion studies. *Philos. Trans. R. Soc. A Math. Phys. Eng. Sci.* **375**, 20160414 (2017).
18. Wang, Z., Seyeux, A., Zanna, S., Maurice, V. & Marcus, P. Chloride-induced alterations of the passive film on 316l stainless steel and blocking effect of prepassivation. *Electrochim. Acta* **329**, 135159 (2020).
19. Yu, X. X., Gulec, A., Cwalina, K. L., Scully, J. R. & Marks, L. D. New insights on the role of chloride during the onset of local corrosion: Tem, apt, surface energy, and morphological instability. *Corrosion* **75**, 616–627 (2019).
20. Maurice, V., Klein, L. & Marcus, P. Atomic structure of metastable pits formed on nickel. *Electrochem. Solid State Lett.* **4**, B1 (2000).
21. Maurice, V. & Marcus, P. Current developments of nanoscale insight into corrosion protection by passive oxide films. *Curr. Opin. Solid State Mater. Sci.* **22**, 156–167 (2018).
22. Hu, C. et al. Improving the intergranular corrosion resistance of 304 stainless steel by grain boundary network control. *Corrosion Sci.* **53**, 1880–1886 (2011).
23. Kim, S. S. h. *Grain boundary character distribution and intergranular corrosion in high-purity aluminum*. Ph.D. thesis, National Library of Canada (2000).
24. Natishan, P. & O'grady, W. Chloride ion interactions with oxide-covered aluminum leading to pitting corrosion: a review. *J. Electrochem. Soc.* **161**, C421 (2014).
25. O'Grady, W. E., Roeper, D. F. & Natishan, P. M. Structure of chlorine k-edge xanes spectra during the breakdown of passive oxide films on aluminum. *J. Phys. Chem. C* **115**, 25298–25303 (2011).
26. Hill, R. J. Crystal structure refinement and electron density distribution in diaspore. *Phys. Chem. Minerals* **5**, 179–200 (1979).
27. Pang, Q., DorMohammadi, H., Isgor, O. B. & Árnadóttir, L. Density functional theory study on the effect of oh and cl adsorption on the surface structure of α-fe2o3. *Comput. Theor. Chem.* **1100**, 91–101 (2017).
28. Pang, Q., DorMohammadi, H., Isgor, O. B. & Árnadóttir, L. The effect of surface vacancies on the interactions of cl with a α-fe2o3 (0001) surface and the role of cl in depassivation. *Corrosion Sci.* **154**, 61–69 (2019).
29. Pang, Q., DorMohammadi, H., Isgor, O. B. & Árnadóttir, L. Thermodynamic feasibility of the four-stage chloride-induced depassivation mechanism of iron. *npj Mater. Degrad.* **4**, 1–5 (2020).
30. Nigussa, K., Nielsen, K., Borck, Ø. & Støvneng, J. Adsorption of h2, cl2, and hcl molecules on α-cr2o3 (0001) surfaces: a density functional theory investigation. *Surface Sci.* **653**, 211–221 (2016).
31. Alavi, S., Sorescu, D. C. & Thompson, D. L. Adsorption of hcl on single-crystal α-al2o3 (0001) surface: a dft study. *J. Phys. Chem. B* **107**, 186–195 (2003).
32. Petrosyan, S., Rigos, A. & Arias, T. Joint density-functional theory: Ab initio study of cr2o3 surface chemistry in solution. *J. Phys. Chem. B* **109**, 15436–15444 (2005).
33. DorMohammadi, H., Pang, Q., Murkute, P., Árnadóttir, L. & Isgor, O. B. Investigation of chloride-induced depassivation of iron in alkaline media by reactive force field molecular dynamics. *npj Mater. Degrad.* **3**, 1–11 (2019).
34. Sarfo, K. O. et al. Density functional theory study of the initial stages of cl-induced degradation of α-cr2o3 passive film. *J. Electrochem. Soc.* **167**, 121508 (2020).
35. Ranea, V. A., Carmichael, I. & Schneider, W. F. Dft investigation of intermediate steps in the hydrolysis of α-al2o3 (0001). *J. Phys. Chem. C* **113**, 2149–2158 (2009).
36. Eng, P. J. et al. Structure of the hydrated α-al2o3 (0001) surface. *Science* **288**, 1029–1033 (2000).
37. Bouzoubaa, A., Diawara, B., Maurice, V., Minot, C. & Marcus, P. Ab initio study of the interaction of chlorides with defect-free hydroxylated nio surfaces. *Corrosion Sci.* **51**, 941–948 (2009).
38. Bouzoubaa, A., Diawara, B., Maurice, V., Minot, C. & Marcus, P. Ab initio modelling of localized corrosion: study of the role of surface steps in the interaction of chlorides with passivated nickel surfaces. *Corrosion Sci.* **51**, 2174–2182 (2009).
39. Todorova, M. & Neugebauer, J. Extending the concept of defect chemistry from semiconductor physics to electrochemistry. *Phys. Rev. Appl.* **1**, 014001 (2014).
40. Zhang, M. & Qi, L. Tuning hydrogen adsorption on pure and doped zno (000 $\bar{1}$) surfaces by a simple electron counting model. *J. Appl. Phys.* **124**, 155302 (2018).
41. Nørskov, J. K. et al. Origin of the overpotential for oxygen reduction at a fuel-cell cathode. *J. Phys. Chem. B* **108**, 17886–17892 (2004).
42. Kennedy, I., Geering, H., Rose, M. & Crossan, A. A simple method to estimate entropy and free energy of atmospheric gases from their action. *Entropy* **21**, 454 (2019).
43. Camaioni, D. M. & Schwerdtfeger, C. A. Comment on "accurate experimental values for the free energies of hydration of h+, oh-, and h3o+". *J. Phys. Chem. A* **109**, 10795–10797 (2005).
44. Taylor, C. D., Li, S. & Samin, A. J. Oxidation versus salt-film formation: competitive adsorption on a series of metals from first-principles. *Electrochim. Acta* **269**, 93–101 (2018).
45. Ke, H., Li, T., Lu, P., Frankel, G. S. & Taylor, C. D. first-principles modeling of the repassivation of corrosion resistant alloys: Part ii. surface adsorption isotherms for alloys and the chloride susceptibility index. *J. Electrochem. Soc.* **167**, 111501 (2020).

46. McGrath, M. J. et al. Calculation of the gibbs free energy of solvation and dissociation of hcl in water via monte carlo simulations and continuum solvation models. *Phys. Chem. Chem. Phys.* **15**, 13578–13585 (2013).
47. Tang, W., Sanville, E. & Henkelman, G. A grid-based bader analysis algorithm without lattice bias. *J. Phys. Condens. Matter* **21**, 084204 (2009).
48. Sanville, E., Kenny, S. D., Smith, R. & Henkelman, G. Improved grid-based algorithm for bader charge allocation. *J. Comput. Chem.* **28**, 899–908 (2007).
49. Henkelman, G., Arnaldsson, A. & Jónsson, H. A fast and robust algorithm for bader decomposition of charge density. *Comput. Mater. Sci.* **36**, 354–360 (2006).
50. Yu, M. & Trinkle, D. R. Accurate and efficient algorithm for bader charge integration. *J. Chem. Phys.* **134**, 064111 (2011).
51. Jain, A. et al. Commentary: The Materials Project: a materials genome approach to accelerating materials innovation. *APL Mater.* **1**, 011002 (2013).
52. Matsui, M. et al. The crystal structure of delta-al (o h)3: neutron diffraction measurements and ab initio calculations. *Am. Mineral.* **96**, 854–859 (2011).
53. Troyanov, S. Crystal structure of titanium(ii) chloroaluminates ti (al cl4)2 and refinement of al cl3 crystal structure. *Zhurnal Neorganicheskoi Khimii* **37**, 266–272 (1992).
54. King, R. B. *Encyclopedia of inorganic chemistry*. https://doi.org/10.1002/0470862106.id264 (John Wiley & Sons, Ltd., 2006).
55. Momma, K. & Izumi, F. *V*ESTA3 for three-dimensional visualization of crystal, volumetric and morphology data. *J. Appl. Crystallogr.* **44**, 1272–1276 (2011).
56. Kresse, G. & Hafner, J. Ab initio molecular dynamics for liquid metals. *Phys. Rev. B* **47**, 558 (1993).
57. Perdew, J. P., Burke, K. & Ernzerhof, M. Generalized gradient approximation made simple. *Phys. Rev. Lett.* **77**, 3865 (1996).
58. Blöchl, P. E. Projector augmented-wave method. *Phys. Rev. B* **50**, 17953 (1994).
59. Kresse, G. & Joubert, D. From ultrasoft pseudopotentials to the projector augmented-wave method. *Phys. Rev. B* **59**, 1758 (1999).
60. Lei, Y., Gong, Y., Duan, Z. & Wang, G. Density functional calculation of activation energies for lattice and grain boundary diffusion in alumina. *Phys. Rev. B* **87**, 214105 (2013).
61. Fabris, S., Nufer, S., Elsässer, C. & Gemming, T. Prismatic σ 3 (101¯ 0) twin boundary in α- al 2 o 3 investigated by density functional theory and transmission electron microscopy. *Phys. Rev. B* **66**, 155415 (2002).
62. Fabris, S. & Elsässer, C. σ 13 (101¯ 4) twin in α- al 2 o 3: A model for a general grain boundary. *Phys. Rev. B* **64**, 245117 (2001).
63. Van Der Geest, A., Islam, M., Couvant, T. & Diawara, B. Energy ordering of grain boundaries in cr2o3: insights from theory. *J. Phys. Condens. Matter* **25**, 485005 (2013).

ACKNOWLEDGEMENTS

We acknowledge support by the Mcubed Seed Funding at the University of Michigan, Ann Arbor, USA (Project ID: 8586). This research was supported in part through computational resources and services provided by Advanced Research Computing at the University of Michigan, Ann Arbor. This work also used the Extreme Science and Engineering Discovery Environment (XSEDE) Stampede2 at the TACC through allocation TG-DMR190035.

AUTHOR CONTRIBUTIONS

A.S., G.C., and L.Q. conceived the research and designed the modeling procedures. A.S. and G.C. performed the calculations. A.S. and L.Q. prepared the manuscript. L.Q. supervised the project. All authors discussed the results and contributed to the manuscript.

COMPETING INTERESTS

The authors declare no competing interests.

ADDITIONAL INFORMATION

Supplementary information The online version contains supplementary material available at https://doi.org/10.1038/s41529-021-00161-w.

Correspondence and requests for materials should be addressed to L.Q.

Reprints and permission information is available at http://www.nature.com/reprints

Publisher's note Springer Nature remains neutral with regard to jurisdictional claims in published maps and institutional affiliations.